

Molecular-Level Study of the Effect of Prior Axial Compression/Torsion on the Axial-Tensile Strength of PPTA Fibers

M. Grujicic, R. Yavari, S. Ramaswami, J.S. Snipes, C.-F. Yen, and B.A. Cheeseman

(Submitted March 2, 2013; in revised form June 22, 2013)

A comprehensive all-atom molecular-level computational investigation is carried out in order to identify and quantify: (i) the effect of prior longitudinal-compressive or axial-torsional loading on the longitudinal-tensile behavior of *p*-phenylene terephthalamide (PPTA) fibrils/fibers; and (ii) the role various microstructural/topological defects play in affecting this behavior. Experimental and computational results available in the relevant open literature were utilized to construct various defects within the molecular-level model and to assign the concentration to these defects consistent with the values generally encountered under “prototypical” PPTA-polymer synthesis and fiber fabrication conditions. When quantifying the effect of the prior longitudinal-compressive/axial-torsional loading on the longitudinal-tensile behavior of PPTA fibrils, the stochastic nature of the size/potency of these defects was taken into account. The results obtained revealed that: (a) due to the stochastic nature of the defect type, concentration/number density and size/potency, the PPTA fibril/fiber longitudinal-tensile strength is a statistical quantity possessing a characteristic probability density function; (b) application of the prior axial compression or axial torsion to the PPTA imperfect single-crystalline fibrils degrades their longitudinal-tensile strength and only slightly modifies the associated probability density function; and (c) introduction of the fibril/fiber interfaces into the computational analyses showed that prior axial torsion can induce major changes in the material microstructure, causing significant reductions in the PPTA-fiber longitudinal-tensile strength and appreciable changes in the associated probability density function.

Keywords effect of compression and torsion, Kevlar, PPTA, tensile properties

1. Introduction

The work described in the present manuscript concerns *p*-phenylene terephthalamide (PPTA) polymeric fibers such as Kevlar®, Twaron®, etc., which are characterized by high specific strength and high specific stiffness. Fibers of this type are often referred to as “ballistic fibers” since they are commonly used in different ballistic- and/or blast-protection systems. The main functional requirement for these systems is a high level of penetration resistance against large kinetic energy projectiles, such as bullets, detonated-mine-induced soil ejecta, improvised explosive devices (IEDs), shell or turbine fragments, etc. Since the behavior/functionality of these protection systems is highly complex, they are nowadays increasingly being designed and developed through an extensive use of computer-aided engineering (CAE) methods and tools. The

utility of these methods and tools depends greatly on the availability of high-fidelity material-constitutive models capable of describing the behavior of fibers and structures under high-rate loading conditions. As argued in our prior work (Ref 1-4), development of such material models requires the recognition and inclusion of the hierarchical/multi-scale architecture of the fibers-based structures as well as of the fibers themselves. Since the present work addresses some of the multi-length-scale aspects of the fibers and fiber-based structures, the main topics overviewed in this section include: (a) the basics of high-performance PPTA fibers; (b) multi-length-scale architecture of the fibers and related structures; and (c) survey of the material models for PPTA fibers and structures used in CAE analyses. It should be noted that the PPTA fibers under investigation are normally used either as: (a) filament constituents in two- or three-dimensional woven-fabric protective structures (e.g., “bulletproof vests”); (b) reinforcements in high-performance (typically, polymer-matrix, “rigid-armor”) composites; or (c) energy-absorbing reinforcements in resin-starved flexible armor-grade composites (Ref 5-8).

1.1 The Basics of Ballistic PPTA Fibers

PPTA fibers fall into the category of aromatic polyamide (polymeric) fibers. The molecular-level structures of the PPTA repeat unit/mer in its *trans* and *cis* stereo-isomeric conformations are shown using a ball-and-stick representation in Fig. 1(a) and (b), respectively. It is seen that the repeat unit consists of two phenylene rings/moieties (C_6H_4RR') connected by an amide linkage ($-CO-NH-$). It should be noted that the

M. Grujicic, R. Yavari, S. Ramaswami, and J.S. Snipes, Department of Mechanical Engineering, Clemson University, 241 Engineering Innovation Building, Clemson, SC 29634-0921; and C.-F. Yen and B.A. Cheeseman, Army Research Laboratory—Weapons & Materials Research Directorate, Aberdeen, Proving Ground, MD 21005-5069. Contact e-mail: gmica@clemson.edu.

Report Documentation Page				Form Approved OMB No. 0704-0188	
Public reporting burden for the collection of information is estimated to average 1 hour per response, including the time for reviewing instructions, searching existing data sources, gathering and maintaining the data needed, and completing and reviewing the collection of information. Send comments regarding this burden estimate or any other aspect of this collection of information, including suggestions for reducing this burden, to Washington Headquarters Services, Directorate for Information Operations and Reports, 1215 Jefferson Davis Highway, Suite 1204, Arlington VA 22202-4302. Respondents should be aware that notwithstanding any other provision of law, no person shall be subject to a penalty for failing to comply with a collection of information if it does not display a currently valid OMB control number.					
1. REPORT DATE 16 JUL 2013		2. REPORT TYPE		3. DATES COVERED 00-00-2013 to 00-00-2013	
4. TITLE AND SUBTITLE Molecular-Level Study of the Effect of Prior Axial Compression/Torsion on the Axial-Tensile Strength of PPTA Fibers				5a. CONTRACT NUMBER	
				5b. GRANT NUMBER	
				5c. PROGRAM ELEMENT NUMBER	
6. AUTHOR(S)				5d. PROJECT NUMBER	
				5e. TASK NUMBER	
				5f. WORK UNIT NUMBER	
7. PERFORMING ORGANIZATION NAME(S) AND ADDRESS(ES) Clemson University, Department of Mechanical Engineering, 241 Engineering Innovation Building, Clemson, SC, 29634				8. PERFORMING ORGANIZATION REPORT NUMBER	
9. SPONSORING/MONITORING AGENCY NAME(S) AND ADDRESS(ES)				10. SPONSOR/MONITOR'S ACRONYM(S)	
				11. SPONSOR/MONITOR'S REPORT NUMBER(S)	
12. DISTRIBUTION/AVAILABILITY STATEMENT Approved for public release; distribution unlimited					
13. SUPPLEMENTARY NOTES					
14. ABSTRACT					
15. SUBJECT TERMS					
16. SECURITY CLASSIFICATION OF:			17. LIMITATION OF ABSTRACT Same as Report (SAR)	18. NUMBER OF PAGES 19	19a. NAME OF RESPONSIBLE PERSON
a. REPORT unclassified	b. ABSTRACT unclassified	c. THIS PAGE unclassified			

trans conformation is almost exclusively found in PPTA molecules, a finding consistent with the PPTA repeat unit molecular structures displayed in Fig. 1(a) and (b). Specifically, Fig. 1(b) shows that, in the case of the *cis* conformation, the rotation about the C-N bond required to convert the *trans* conformation into the *cis* conformation, is opposed by the steric repulsion between the hydrogen atoms on the adjacent aromatic rings. The prevalence of the *trans* conformation in the PPTA molecules is generally linked to the fact that these molecules typically acquire a lower-energy stretched-out/extended shape. The presence of large numbers of nearly parallel molecules, in turn, enables the fiber to take full advantage of the linear character of the molecular backbone structure and to further lower its potential energy by forming crystalline PPTA fibrils.

Due to a large difference in electronegativity between oxygen and hydrogen, the electron charge density within the PPTA unit cell becomes increased around the oxygen atoms and decreased around the hydrogen atoms, giving rise to the formation of strong dipoles. This condition typically results in the formation of (strong) hydrogen bonds. It is well-established that hydrogen bonding in the lateral direction between parallel PPTA molecules/chains is responsible for the formation of “sheet-like” structures (observed in PPTA fibrils/fibers). As will be established in more detail later, PPTA fibers consist of smaller units called fibrils, elongated and running coaxially with the fibers. PPTA fibrils are commonly found to have a crystalline structure consisting of stacked sheets, with the orientation of the stacked sheets varying between different fibrils. As mentioned above, (strong) hydrogen bonding plays the dominant role in the formation of the sheets. On the other hand, (weak) van der Waals interactions and the formation of

π -type molecular orbitals are mainly responsible for inter-sheet bonding.

The properties of PPTA fibrils/fibers are greatly affected by the presence, the type and the concentration of various crystallographic and morphological defects/flaws (like the stacking faults, mentioned above). The type, size/potency, and the concentration of these flaws are a sensitive function of the PPTA synthesis and fiber fabrication processes (Ref 9-11). A summary of the PPTA fibril most common defects, their dimensionality, their cause, ways of reducing their number density and their typical concentrations, is provided in Table 1 (Ref 1-4).

1.2 Multi-length-scale Architecture of PPTA-Fiber-Based Structures

Detailed examination of PPTA fibrils/fibers and related protective structures carried out in our recent work (Ref 1-4) revealed their high morphological and behavioral complexity which is mainly attributed to: (a) the presence of a hierarchical, multi-length-scale architecture; (b) their mechanical response which is often quite non-linear and path and rate/time-dependent; and (c) the operation of various phenomena/processes (e.g., fibril/fiber damage, highly localized deformation and the associated formation of kink/deformation bands, filament twisting, inter-filament friction and sliding, etc.). The term “filament” is used here to denote thread-like entities (typically fibers or yarns) employed in the construction of the protective systems. PPTA fibers are typically produced by a polymer-spinning process while the yarns are produced by assembling the fibers into nearly parallel bundles, applying a slight twist to the bundle about the yarn axis and/or wrapping fibers around the bundle to hold the fibers together.

In our recent work (Ref 1, 2), an attempt was made to help identify distinct length scales within the protective structures consisting of polymer-matrix-composite materials reinforced with PPTA filaments. Within that attempt, eight distinct length scales were identified and analyzed in great detail. While a detailed description of these length scales will not be presented here, a schematic of the material microstructure/architecture along with the labels used to denote the main microstructural constituents is shown in Fig. 2(a)-(h), respectively, for each of the length scales. The present work mainly deals with the PPTA-based materials at the three smallest length scales, i.e., at the fiber, fibril, and molecular-level length scales.

1.3 Material Models of PPTA Protective Structures for Use in CAE Analyses

Design and development of the PPTA-fiber-based ballistic-/blast-protection systems is traditionally carried out using legacy knowledge, empiricism, and extensive “make-and-test” procedures. This approach is not only associated with higher cost, but often entails significantly longer lead times. Consequently, it has gradually become complemented (and partly replaced) by the appropriate cost- and time-efficient CAE analyses (Ref 12, 13). However, as was shown in our prior work (Ref 14) the utility of these analyses is greatly dependent on the availability of high-fidelity constitutive models for the materials which are used in the construction of the PPTA protective structures. As demonstrated in our prior work (Ref 3), the PPTA material-constitutive models currently in use are not fully capable of accounting for the response of the subject material to high deformation rate, large strain, high pressure loading conditions

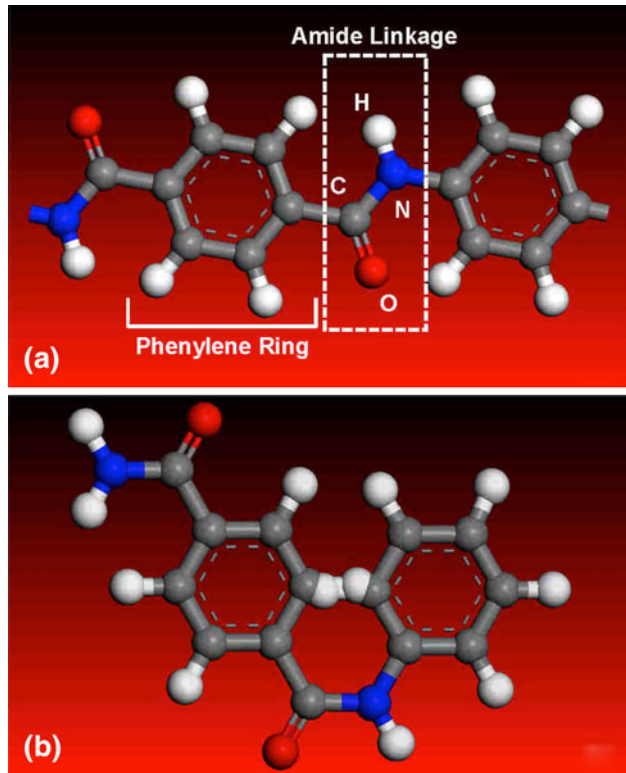


Fig. 1 (a) *Trans*-molecular and (b) *Cis*-molecular conformations in typical PPTA-based polymeric-material chains/molecules

Table 1 Classification of the most common defects found in PPTA fibers

Defect class	Defect type	Cause(s)	Defect formation prevention	Number density range
Isolated chain ends (point defect)	-COOH	H ₂ SO ₄ catalyzed hydrolysis causing PPTA chain scission. Na ⁺ deficiency with respect to complete neutralization of side/end acidic groups.	Use concentrated H ₂ SO ₄ for dope preparation. Shorten the fiber wash time	0.35 per PPTA chain for each defect(a) (~350 ppm-mass-based)
	-NH ₂	H ₂ SO ₄ catalyzed hydrolysis causing PPTA chain scission. Na ⁺ deficiency with respect to complete neutralization of side/end acidic groups	Use higher concentration NaOH solution	0.35 per PPTA chain for each defect(a) (~350 ppm-mass-based)
	-COO ⁻ Na ⁺	COOH neutralization with Na ⁺	No remedy required since this is one of the preferred chain ends	1.1 per PPTA chain(a) (~1100 ppm-mass-based)
	-NH ₃ ⁺ HSO ₄ ⁻	Sulfonation of the NH ₂ chain ends	Increase the H ₂ SO ₄ removal and neutralization rate	0.2 per PPTA chain(a) (~200 ppm-mass-based)
	-SO ₃ H	Exposure of PPTA in the dope to concentrated H ₂ SO ₄ (sulfonation)	Reduce the H ₂ SO ₄ concentration in the dope	~1300 ppm (mass-based)
Side Groups (point defect)	-SO ₃ ⁻ Na ⁺	Neutralization of sulfonic acid side groups by NaOH	Remedy may not be required since this side group improves fiber longevity. However mechanical performance may be compromised	~2500 ppm (mass-based)
Voids and Interstitials (point defects)	Microvoids	Swelling induced by hydration of intra-fibrillar Na ₂ SO ₄	Increase the extent of sodium salt dissolution by prolonged exposure of fibers to boiling water	~150 ppm (mass-based)
	Mobile trapped H ₂ SO ₄	Non-neutralized or unwashed intra-fibrillar H ₂ SO ₄	Thorough washing in hot solvent aqueous bath	~70 ppm (mass-based)
Defect bands (planar defects)	-NH ₃ ⁺ HSO ₄ ⁻ agglomerated chain ends	Coulombic attraction induced clustering of ion-terminated chain ends	The phenomenon is not well understood so no remedy is obvious	One band every 40-60 nm of fibril (ca. 3000 ppm-mass-based)
(a) Extruded fibers				

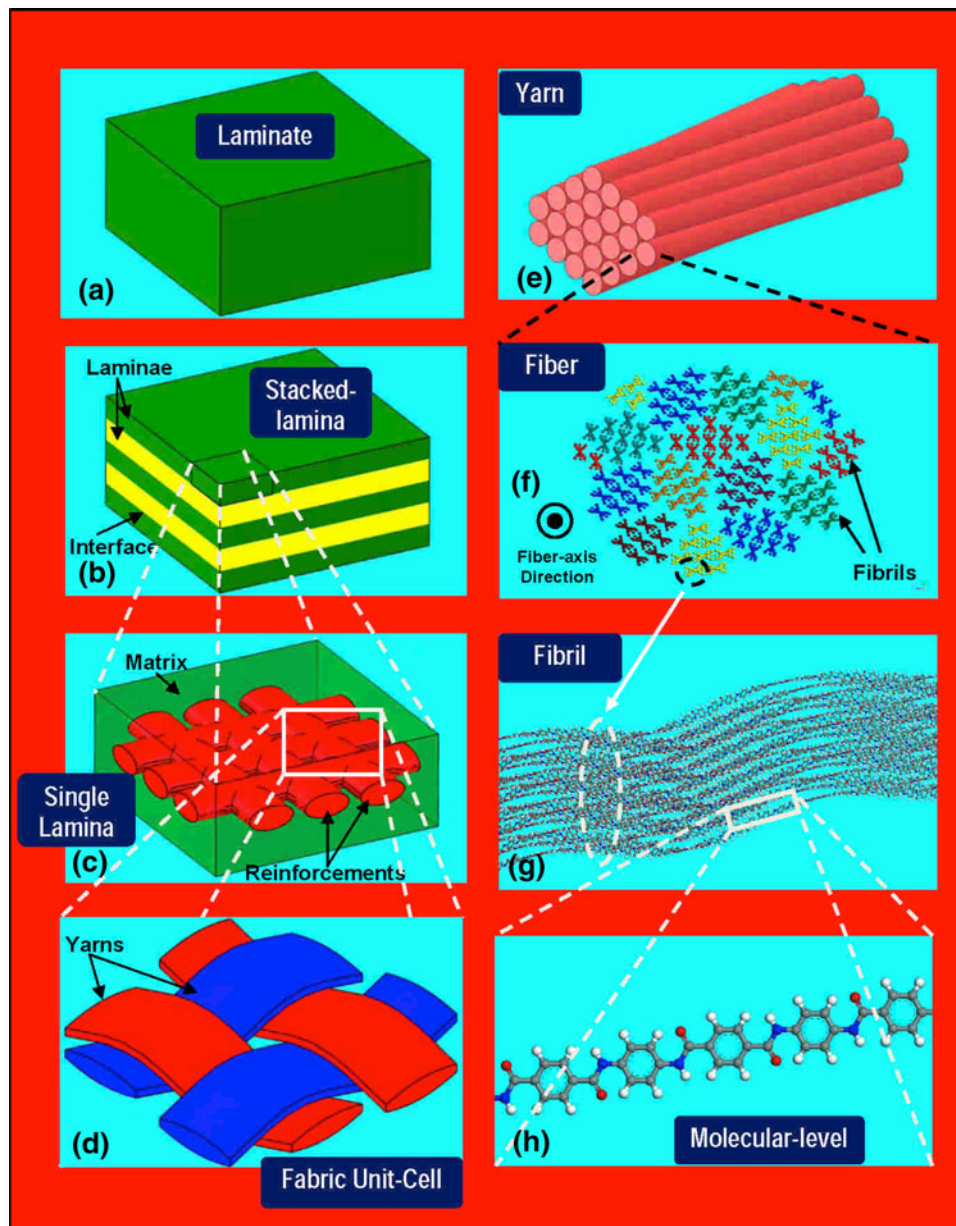


Fig. 2 Eight length scales encountered in the study of polymer-matrix composite materials reinforced with high-performance fiber-based structures

(the type of loading conditions typically encountered during projectile or blast impact events) or for the effect of prior treatment/handling of the constituent fiber materials (as well as the effect of the overall protective structure manufacturing process). It is generally believed that elimination of the deficiencies of the current PPTA material models must start with the recognition of and the inclusion of various phenomena and processes occurring at different length scales and their effects on the overall behavior/performance of the subject material. In our recent work (Ref 1-4), the following improvements were made in the PPTA material-constitutive models: (i) the effect of various fiber- and sub-fiber-length-scale microstructural features (including the defect structure) on the material dynamic response is accounted for; and (ii) inelastic deformation effects associated

with transverse loading and their coupling to the longitudinal mechanical properties of the PPTA fibers are incorporated. In the present work, an attempt is made to identify and quantify the effects of prior longitudinal-compressive and/or axial-torsional loading on the tensile behavior of the PPTA fibers so that the effect of fiber handling during PPTA-structure fabrication can be accounted for (Ref 15).

1.4 Main Objective

The main objective of the present study is to extend our prior molecular-type simulation work (Ref 1-4) in order to: (i) provide insight into the effect of prior longitudinal compression and/or axial torsion of the single PPTA fibrils on the

longitudinal strength of the fibrils and the associated fibers and (ii) to reveal the role of various microstructural and topological molecular-/fiber-level defects on the effect of prior longitudinal-compressive/axial-torsional loading on the longitudinal-tensile response of the PPTA fibrils.

2. Prior Compression/Torsion and Fiber Axial Strength

In this section, a comprehensive summary is provided of the main experimental findings dealing with the effect of prior longitudinal compression and/or axial torsion on the longitudinal-tensile strength of the single PPTA fibers. Examination of the open-domain literature revealed the presence of one report, Ref 16 dealing with the axial compressive behavior of single PPTA fibers, two sources, Ref 15, 17 reporting the behavior of single PPTA fibers under axial torsion, and one study, Ref 15 dealing with the effect of prior axial compression/torsion on the subsequent longitudinal-tensile behavior of single PPTA fibers. In the remainder of this section, a brief summary is provided with the main findings obtained in the aforementioned references. For clarity, this summary is divided into three separate sections.

2.1 Dobb et al. (Ref 16)

Dobb et al. (Ref 16) carried out longitudinal compression tests on single PPTA fibers and examined the fiber microstructure before and after testing in order to identify microstructural changes responsible for the inferior axial-compressive strength of the fibers. The main findings of Dobb et al. can be summarized as: (a) the inferior longitudinal compression of the single PPTA fibers is related to the formation and propagation of kink bands; (b) formation and propagation of the kink bands has been found not to be closely related to the presence of the aforementioned accordion-style pleats; (c) the main mechanism responsible for the formation of kink bands is the relatively weak van der Waals inter-sheet bonding, and the associated weak lateral support experienced by the PPTA sheets. These conditions can lead to the phenomena such as localized shear, delamination, and buckling, all of which play an important role in the formation of kink bands; and (d) the presence of the crystalline structure within the PPTA fibrils promotes the formation of the kinks through the coordinated motion of the well-organized PPTA chain segments.

2.2 Cheng et al. (Ref 17)

Chen et al. (Ref 17) carried out a series of mechanical tests, including axial torsion, on single PPTA fibers. The main findings of their work can be summarized as follows: (a) in the small-deformation range, single PPTA fibers behave as linear-elastic transversely isotropic materials which are characterized by five (independent) elastic stiffness constants/moduli; (b) using a version of the torsional-pendulum single-fiber-test apparatus, Chen et al. established that the relevant elastic constant, i.e., the longitudinal shear modulus, is a stochastic quantity. Furthermore, it was found that the moments of the probability density function (e.g., first moment = mean, second moment = standard deviation, etc.) for the longitudinal shear modulus are dependent on the single fiber gage length, suggesting that previously discussed morphological and

crystallographic defects within the PPTA fibers affect fiber properties; (c) at sufficiently high torsional strains, single PPTA fibers fail, mainly via the fibrillation failure mechanism.

2.3 DeTeresa et al. (Ref 15)

DeTeresa et al. (Ref 15) carried out a systematic experimental investigation of the effect of prior axial compression and/or axial torsion on the longitudinal tensile strength of single PPTA fibers. The mechanical tests were supplemented by the optical and scanning electron microscopies in order to relate changes in the fiber microstructure induced by prior (longitudinal-compressive or axial-torsional) deformation to the observed losses in the fiber longitudinal tensile strength. The results obtained by DeTeresa et al. can be summarized as follows: (a) prior longitudinal compression produces regularly spaced helical kink bands in the single PPTA fibers; (b) the introduction of these bands lowers the fiber longitudinal-tensile strength. Typically, a loss of ca. 10% in the fiber longitudinal-tensile strength is associated with the prior application of 3% longitudinal-compressive strain; (c) small axial-torsional strains (ca. < 10%) are found to be fully recoverable upon loading and not to induce any noticeable damage to the tested fiber. In sharp contrast, large axial-torsional strains (ca. > 10%) are found to give rise to either partial fibrillation (which is accompanied by an unrecoverable/residual torsional strain upon unloading) or complete fibrillation (i.e., torsional failure); (d) the onset of fibrillation coincides with the onset of degradation in the fiber longitudinal-tensile strength. The loss of longitudinal-tensile strength due to prior axial-torsional loading is quite severe and, typically, an increase in the torsional strain from 10 to 30% approximately halves the fiber longitudinal-tensile strength; and (e) the fibrillation damage/failure mechanism has been linked with weak inter-fibril van der Waals bonding.

3. All-Atom Molecular-Level Computational Analysis

As mentioned earlier, all-atom molecular-level computational methods have been employed in the present work in order to: (a) provide additional insight into the relationship between prior longitudinal compression and/or axial torsion, and the longitudinal-tensile strength of single PPTA fibers; and (b) establish the extent to which this relationship is affected by the presence, type and concentration of various crystallographic and morphological defects. In general, the formulation of an all-atom molecular-level modeling and simulation problem requires, at a minimum, specification of the following five items: (a) a molecular-level computational model consisting of atoms, ions, moieties, functional groups, molecular chains, crystalline unit cells, etc.; (b) a set of force-field functions, which describe various bonding and non-bonding interactions between the constituents of the molecular-scale model; (c) types and sequence of the computational method(s) to be employed in the simulation; (d) formulation of the physical problem being investigated/simulated; and (e) specification of the methods and procedures to be used in the post-processing data-reduction analysis. A brief overview of these items is provided in the remainder of this section.

3.1 Computational Model

To gain insight into the effect of prior longitudinal compression and/or axial torsion on longitudinal-tensile strength of single PPTA fibers, a relatively large number of molecular-level computational models containing various perfect-crystal PPTA conformations and different microstructural/topological defects were used in the present work. Figures 3(a), (b) and 4(a)-(d) depict several examples of the computational

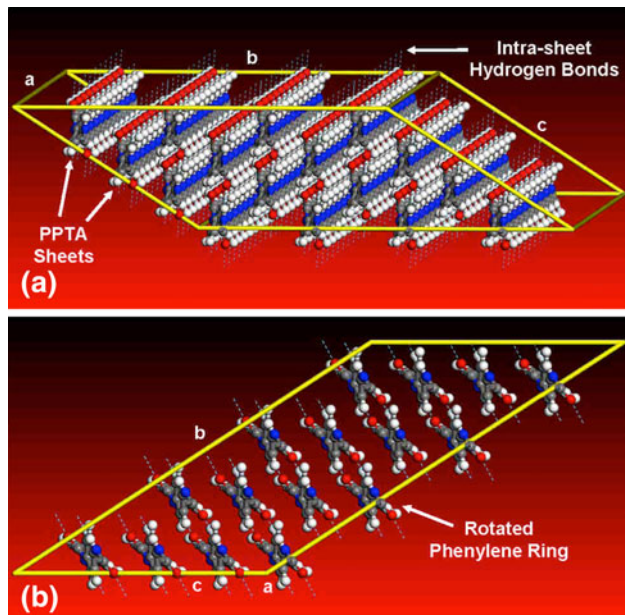


Fig. 3 Two close-up views of the computational unit cell containing a perfect PPTA crystalline structure

models used. In Fig. 3(a) and (b), two close-up views of the computational unit cell containing a perfect PPTA crystalline structure are shown. In addition, important topological/microstructural features such as phenylene rings, PPTA sheets, and intra-sheet hydrogen bonding are labeled in this figure. Figure 4(a)-(d), on the other hand, show, respectively, four computational unit cells, each containing a single defect from one of the four defect classes, as listed in Table 1. Specifically, the following defects are depicted: (a) isolated -COOH group (a chain-end defect), Fig. 4(a); (b) isolated -SO₃H group (a side-group defect), Fig. 4(b); (c) isolated mobile H₂SO₄ molecules (an interstitial defect), Fig. 4(c); and (d) a defect band (a planar defect), Fig. 4(d). It should be noted that, for improved clarity, atoms within defects are enlarged and highlighted in yellow in Fig. 4(a)-(c), and enlarged in Fig. 4(d). All the computational models analyzed in the present work were constructed using Visualizer (Ref 18) and Amorphous Cell (Ref 19) molecular microstructure pre-processing tools.

Construction of the defect-free PPTA computational material models was carried out under the following conditions: (a) the fibers are considered to be bundles of parallel, fully crystalline fibrils; (b) the crystalline structure of the fibrils is modeled as a stack of parallel PPTA sheets, with each sheet containing molecular chains aligned in the fibril/fiber-axis direction. The inter-chain bonding within the sheets is assumed to be of the hydrogen-bond character while van der Waals bonding is assumed to hold the adjacent sheets together; (c) to account for the fact that the vast majority of the molecules inside PPTA fibrils are fully surrounded by other chains: (i) a bulk-like environment is created for the “fibril material” using the concept of the unit-/computational-cell and the periodic boundary conditions. For ease of construction, the computational cells used were all of the monoclinic parallelepiped shape, with a non-90° α -angle, i.e., the angle between the computational cell edges b and c . The edge a of the

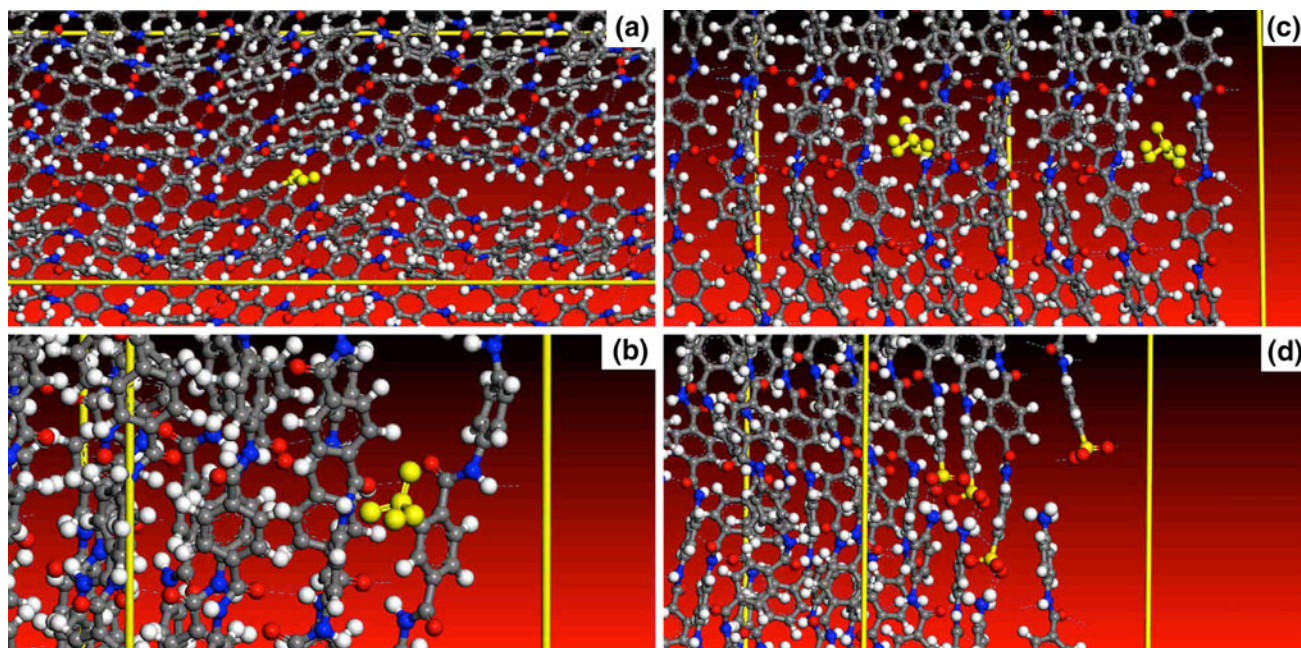


Fig. 4 Examples of the computational models containing defective PPTA crystalline structures: (a) isolated -COOH group (a chain-end defect), (b) isolated -SO₃H group (a side-group defect), (c) isolated mobile H₂SO₄ molecules (an interstitial defect), and (d) a defect band (a planar defect). For clarity, atoms within defects are enlarged and highlighted in yellow in (a)-(c), and enlarged in (d) (Color figure online)

computational cell is aligned with the fiber axis (i.e., with the fibril axial direction) while edge b is aligned with the PPTA-sheet normals. It should be noted that despite the fact that a monoclinic parallelepiped-shaped computational cell was used, the underlying PPTA crystalline material possesses an orthotropic symmetry; and (ii) application of the periodic boundary conditions in the fibril axial direction yields infinitely long fibrils while the application of these conditions in the other two directions provides a bulk-like environment to each PPTA molecule within the fibril; and (d) sheet-pleating was not explicitly accounted for since its periodic length substantially increases the size of the PPTA computational cells used.

As far as the computational cells containing imperfect crystalline PPTA are concerned, the following procedures are employed to create defects within the initially perfect crystalline material: (a) chain scission followed by the attachment of the appropriate chain-end groups, in the case of chain-end defects; (b) chain-side functionalization, in the case of side-group defects; (c) insertion of nitrogen molecules, in the case of (air-filled) voids; (d) insertion of H_2SO_4 molecules, in the case of interstitials; and (e) scission of a number of adjacent chains in a plane orthogonal to the fibril axis, in the case of defect bands. Additional details regarding the molecular-level microstructures and topologies associated with each of these defects could be found in our prior work (Ref 1, 2).

3.2 Force Fields

The behavior of a material system at the molecular-level is governed by the appropriate force fields which define functional relationships between different components of the constituent particle (atom/ion) interaction energies and the particle position, nature, charge, and state of bonding. In the present work, the so-called “COMPASS” (Condensed-phase Optimized Molecular Potentials for Atomistic Simulation Studies) force field is used (Ref 18, 19). This force field is of an ab initio type, since most of its parameters were determined by matching the predictions made by the ab initio quantum mechanics calculations to the condensed matter experimental data. It is, hence, considered quite accurate and of high fidelity. The key functional relationship within a force field is the mathematical expression that defines the potential energy of the system of interacting particles as a function of their chemical type and their topological environment. Within the COMPASS force field, the potential energy of a system of interacting atoms/ions is expressed as a sum of a valence (covalent-bonding) term, a cross (atomic-environment-dependent bonding) term, and a non-bond van der Waals and Coulombic (including hydrogen bonding) pair interaction term. A summary of the COMPASS force field functional relations can be found in our previous work (Ref 1) and, hence, will not be provided here. However, since hydrogen bonding plays an important role in the formation of the crystalline structure and, thus, the mechanical behavior of the PPTA fibers, it is described in more detail in the remainder of this section.

As mentioned earlier, due to a large difference in the electronegativity between oxygen and hydrogen and the presence of lone electron pairs within oxygen, strong hydrogen bonds are formed between adjacent molecules within the same PPTA sheet. Within the molecular-level simulations carried out in the present work, hydrogen bonds are formed between the atoms adaptively when the following criteria are satisfied: (a)

one of the atoms involved is hydrogen, which is single-bonded to another atom (N, in the present case), on the same molecule, which can act as a hydrogen-bond donor; (b) the second atom considered (O, in the present case) is capable of acting as a hydrogen-bond acceptor, i.e., it contains at least one lone electron pair; (c) the distance between the hydrogen atom and the hydrogen-bond acceptor atom is smaller than, or equal to, a predefined upper bound (0.25 nm, in the present case); (d) the angle formed by the hydrogen-bond donor atom, hydrogen atom and the hydrogen-bond acceptor atom is greater than, or equal to, a predefined lower bound (90° in the present case); and (e) when both the hydrogen atom and hydrogen-acceptor atom are within the same molecule, they are separated by at least four nearest neighbor atomic shells.

As mentioned earlier, hydrogen bonding contributes to the so-called “non-bond” portion of the material potential energy function. Typically, this contribution is expressed using the so-called “10-12 Lennard-Jones” potential (Ref 20) in the form:

$$E_{H-\text{bond}} = \frac{A}{r_{ij}^{12}} - \frac{B}{r_{ij}^{10}} \quad (\text{Eq 1})$$

where A and B are coefficients with units of kcal/mol \AA^{12} and kcal/mol \AA^{10} , respectively; and r_{ij} is the distance between the hydrogen atom i and the hydrogen-bond-acceptor atom j in angstroms.

3.3 Computational Method

To gain insight into the mechanical response of a perfect and defective crystalline PPTA, molecular statics and molecular dynamics simulations were conducted on the computational cells described earlier. All the calculations carried out in the present work employed Discover (Ref 21) (an atomic simulation program from Accelrys). A brief description of the two molecular-level computational methods employed is provided below.

The molecular statics method is effectively a constrained optimization procedure within which the potential energy of the computational cell (the objective function) is minimized with respect to the positions of the constituent atoms and ions (the design variables) while ensuring that the periodic conditions (i.e., long-range order of the subject material) are retained. The potential energy minimization within Discover (Ref 21) is carried out by applying sequentially and adaptively several minimization algorithms in order to attain an optimal combination of computational efficiency and robustness.

Within the molecular dynamics approach, the following two-step procedure is repeated at each (0.1-1.0 fs long) time step: (a) the negative gradient of the potential energy with respect to the atom/ion positions is first used to compute the current forces acting on each atom/ion; (b) then, the associated Newton's equations of motion are integrated numerically in order to compute the acceleration associated with each atom/ion and to, in turn, update the velocity and the position of each atom/ion. To ensure that the system is in a state of equilibrium and is not subjected to any thermodynamic/mechanical fluxes, only equilibrium molecular dynamics methods were used in the present work. Within these methods, the system of interacting atoms/ions under consideration is coupled to a (infinite-extent, external) surrounding (e.g., a constant temperature reservoir, in the present case). In the present work, NVT equilibrium molecular dynamics

simulations are employed (where N is the (fixed) number of atoms/ions within the computational cell, V is the computational cell volume (also fixed), and T ($= 298$ K) is the fixed temperature).

3.4 Problem Formulation

As mentioned earlier, the problem analyzed in the present work involves the mechanical response of PPTA fibers subjected first to either longitudinal compression or axial torsion and subsequently subjected to longitudinal tension. Typically, PPTA fiber diameter is on the order of $10\text{ }\mu\text{m}$, and thus 10^3 - 10^4 times larger than the size of a prototypical molecular-level computational cell, analyzed in the present work. As established earlier, fibers are composed of elongated, coaxial, crystalline fibrils with lateral dimensions being one to two orders of magnitude smaller than those of the fibers. Taking these findings into consideration, one can conclude that a PPTA material domain of the size equal to that of the computational cell has the highest probability of residing within a single PPTA fibril. That is the reason that, within the present work, most of the computational cells are assumed to be perfect or imperfect single crystalline. As will be discussed in the next section, in order to explain some of the findings related to the effect of prior axial torsion, additional computational cells containing PPTA bi-fibrils will have to be constructed and analyzed.

Considering the above, the problem analyzed within the present work involves: (i) prelude longitudinal compression or simple shear on planes normal to the fibril axis (the typical strain deformation mode associated with axial torsion); and (ii) subsequent longitudinal tension. Two modes of simple shear are considered, one in the direction orthogonal to the PPTA sheets, and the other in a direction coplanar with the PPTA sheets. Both the prelude and the final deformations were applied in small increments and each incremental deformation is followed by the computational cell energy minimization and extended (ca. 40 ns) molecular dynamics simulation runs. The results obtained are post-processed using the procedures described in the next section in order to establish the role of the prelude deformation mode and extent on the longitudinal tensile strength of the single PPTA fibrils/fibers (in the presence or in the absence of morphological/crystallographic defects).

The aforementioned procedure for incremental deformations, including molecular statics, energy minimization and prolonged molecular-dynamics-based thermal equilibration, is conducted through the use of a Discover input file (Ref 21). This file is written in the Basic Tool Command Language (BTCL), which enabled the use of a scripting engine that provides detailed and precise control of simulation tasks.

3.5 Post-processing Data-Reduction Analysis

The molecular-level computational results obtained are used to assess the corresponding material stiffness and strength parameters/values. The post-processing data-reduction procedures used in the course of assessment of these PPTA fibril/fiber mechanical properties from the molecular-level computational results are described in the remainder of this section.

3.5.1 Elastic Stiffness. Within the molecular-level computational framework, molecular statics and/or molecular dynamics approaches can be used to determine the components

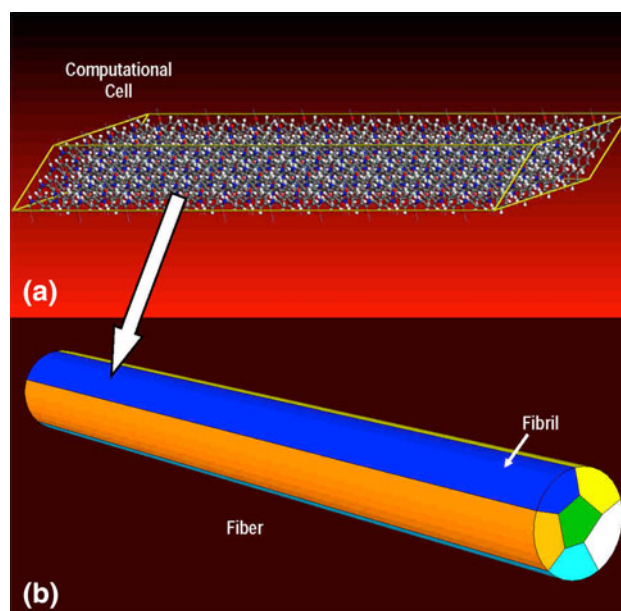


Fig. 5 Topological relationship between: (a) a prototypical PPTA computational cell used in the present work and (b) PPTA fibrils within a single fiber

of the fourth-order elastic stiffness tensor. The two types of approaches are briefly described in the remainder of this section.

When the second-order elastic stiffness tensor is assessed using the molecular statics results, the contributions of the finite-temperature thermal expansion and the vibrational/configurational entropic effects to the system free energy are not taken into account. Consequently, the resulting elastic stiffness tensor, defined as a second-order derivative of the system's free energy (assessed at the equilibrium, i.e., the minimum energy state of the system under investigation) with respect to the unit cell strain components, reflects the behavior of the material in question under small deformations at zero absolute temperature. Since the aforementioned finite-temperature effects can make a significant contribution to the elastic stiffness tensor, it is generally not justified to neglect them. That is the reason that a molecular-dynamics-based elastic stiffness computational procedure which accounts for the aforementioned thermal and entropic effects is utilized in the present work. A brief description of this procedure is provided in the remainder of this section. However, before describing this procedure, it should be noted that the computational cell edges are used to construct the material-based coordinate system within which the elastic stiffness tensor (as well as the stress and strain) are defined. That is, the x_1 -direction is aligned with the computational cell edge a , i.e., with the fibril longitudinal direction, the x_2 -direction is aligned with the PPTA sheets normal, and the x_3 -direction (lies in the plane of the PPTA sheets and is orthogonal to the PPTA molecule backbone) is defined as the cross product of x_1 and x_2 .

Within the approach used, the elastic stiffness tensor is determined using the prolonged equilibrium molecular dynamics simulation results to calculate the time-based correlation functions between different stress and strain components. The components of the strain, ϵ_{ik} , and stress, σ_{nj} , second-order tensors are calculated, respectively, as:

$$\varepsilon_{ik} = \frac{1}{2} \left(h_{nl} \langle h \rangle_{lk}^{-1} h_{np} \langle h \rangle_{pi}^{-1} - \delta_{ik} \right) \quad (\text{Eq 2})$$

$$\sigma_{nj} = \frac{1}{V} \left\{ \sum_a \frac{(p_a)_n (p_a)_j}{m_a} + \sum_{a>b} \frac{\partial E}{\partial r_{ab}} \frac{(x_{ab})_n (x_{ab})_j}{r_{ab}} \right\} \quad (\text{Eq 3})$$

where h_{ij} is an (i, j) element of a second-order tensor defining the three unit cell edge vectors within the reference frame, δ_{ij} is the Kronecker delta, V is the computational cell volume, p_a is the momentum of atom a , m_a is the mass of atom a , E denotes the potential energy function, r the inter-particle spacing, x the inter-particle position vector, and angular brackets are used to denote the time/ensemble average of a given quantity.

The components of the elastic stiffness fourth-order tensor, C_{iklm} , are next computed using the following equations:

$$C_{iklm} = \frac{k_B T}{\langle V \rangle} \langle \varepsilon_{ik} \varepsilon_{lm} \rangle^{-1} \quad (\text{Eq 4})$$

or

$$C_{iklm} = \langle \varepsilon_{ik} \sigma_{nj} \rangle \langle \varepsilon_{nj} \varepsilon_{lm} \rangle^{-1} \quad (\text{Eq 5})$$

where k_B is the Boltzmann's constant, T is the absolute temperature, and $\langle a_{ik} b_{lm} \rangle$ is the time-based correlation function between the (i, k) -component of a second-order tensor a and the (l, m) -component of a second-order tensor b .

The fourth-order elastic stiffness tensor C_{iklm} is then converted, using the Voigt notation, into a 6×6 elastic stiffness matrix, C . The results obtained in the present work generally showed that the C matrix contains nine independent elements, suggesting that the PPTA-crystal structure possesses orthotropic symmetry.

Since it is customary practice to work with the engineering moduli rather than with the elastic stiffness constants, the corresponding three Young's moduli (E_{11} , E_{22} , E_{33}), three shear moduli ($G_{12} = G_{21}$, $G_{13} = G_{31}$, $G_{23} = G_{32}$), and three Poisson's ratios ν_{12} ($= \nu_{21} \times E_{11}/E_{22}$), ν_{13} ($= \nu_{31} \times E_{11}/E_{33}$) and ν_{23} ($= \nu_{32} \times E_{22}/E_{33}$), are next determined using standard functional relations, e.g., Ref 22.

3.5.2 Longitudinal-Tensile Strength. While three distinct deformation modes, i.e., longitudinal compression, simple shear, and longitudinal tension, are employed in the molecular-simulation procedures described earlier, only longitudinal-tensile strength was assessed using the simulation results. The reason for this is that the main objective of the present work is to assess sensitivity of the longitudinal-tensile strength of single PPTA fibers to the prior longitudinal compression or axial torsion as well as to the presence, type, and concentration of various morphological and crystallographic defects. In addition, since the problem of single PPTA fiber transverse

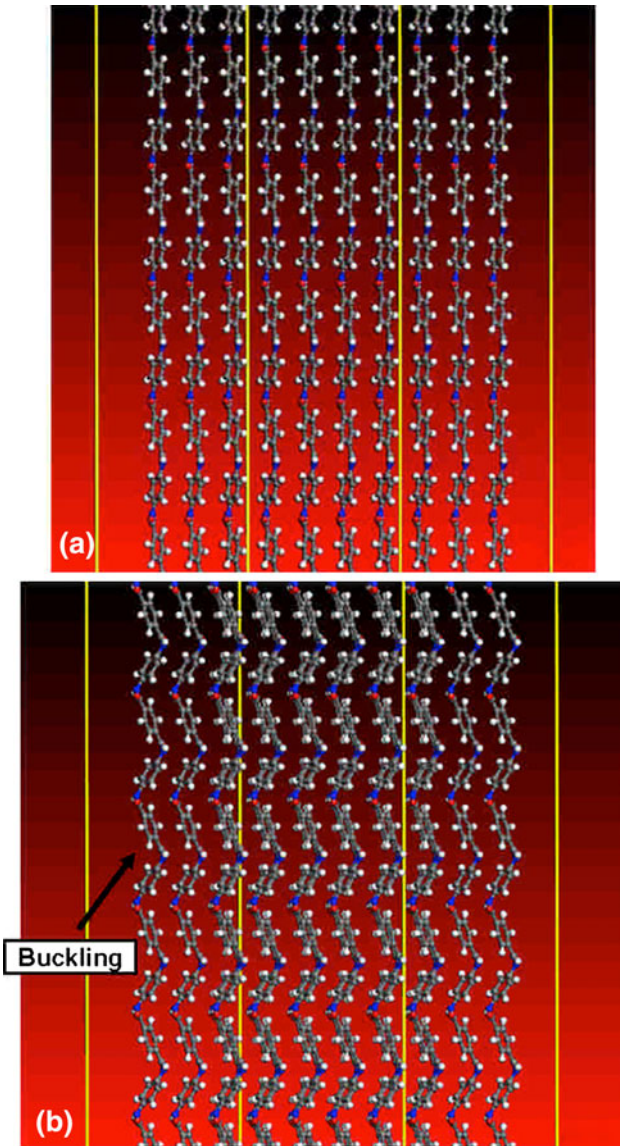


Fig. 6 Molecular-level microstructure in perfect PPTA crystal: (a) before and (b) during the application of axial compressive strain of -0.05

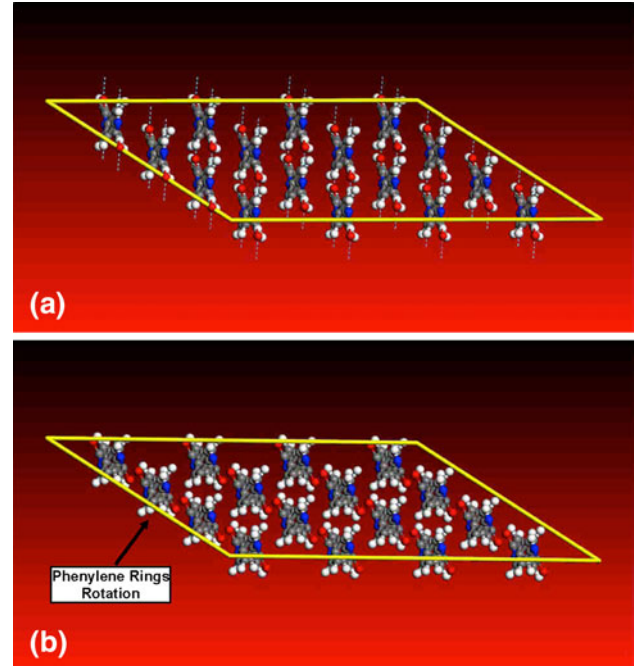


Fig. 7 Molecular-level microstructure in perfect PPTA crystal: (a) before and (b) during the application of simple shear strain of 0.1

strength was addressed in our recent work (Ref 4), the same component of the fiber strength did not need to be computed and analyzed here. Tensile strength in the longitudinal direction of the PPTA fibrils is determined by subjecting the unit cell to longitudinal tensile deformation in the x_1 -direction while allowing for the operation of the Poisson's effects in the x_2 - and x_3 -directions. Meanwhile, the normal stress in the x_1 -direction is computed via Eq 3 as well as its rate of increase with an increase in the longitudinal tensile strain. The longitudinal-tensile strength of the single PPTA fibril is then set equal to the value of the corresponding normal stress at which the rate of stress increase with increase in strain begins to decline "appreciably" (denoting the onset of inelastic deformation).

4. Results and Discussion

In this section, the results of the all-atom molecular-level computational analyses used to assess: (i) the effect of prior longitudinal compression and/or axial torsion of the single

PPTA fibrils on the longitudinal strength of the fibrils and the associated fibers; and (ii) the role of various microstructural and topological molecular-/fiber-level defects on the effect of prior longitudinal-compressive/axial-torsional loading on the longitudinal-tensile response of the PPTA fibrils, are presented and discussed.

Before the results are presented and discussed, it is important to establish a geometrical/kinematic relationship between the computational cells utilized in the present work and a typical PPTA fibril/fiber architecture. This relationship is schematically depicted in Fig. 5(a) and (b). In Fig. 5(a), a schematic of a prototypical PPTA computational cell used in the present work is depicted. As mentioned earlier, the material region covered by the computational cell is assumed to reside within a single PPTA fibril. As seen in Fig. 5(b), which depicts a single PPTA fiber, such a fiber consists of a number of nearly parallel fibrils. Within each fibril: (i) the fibril axis lies within the PPTA sheets; (ii) the fibril axis is (nearly) coincident with the fiber axis; and (iii) different fibrils merely differ in the orientation of the sheet normals (while the sheet normal in each fibril is orthogonal to the fibril/fiber axis). Based on the computational-cell/fibril/fiber kinematic relationship depicted in Fig. 5(a) and (b), it is clear that the present computational

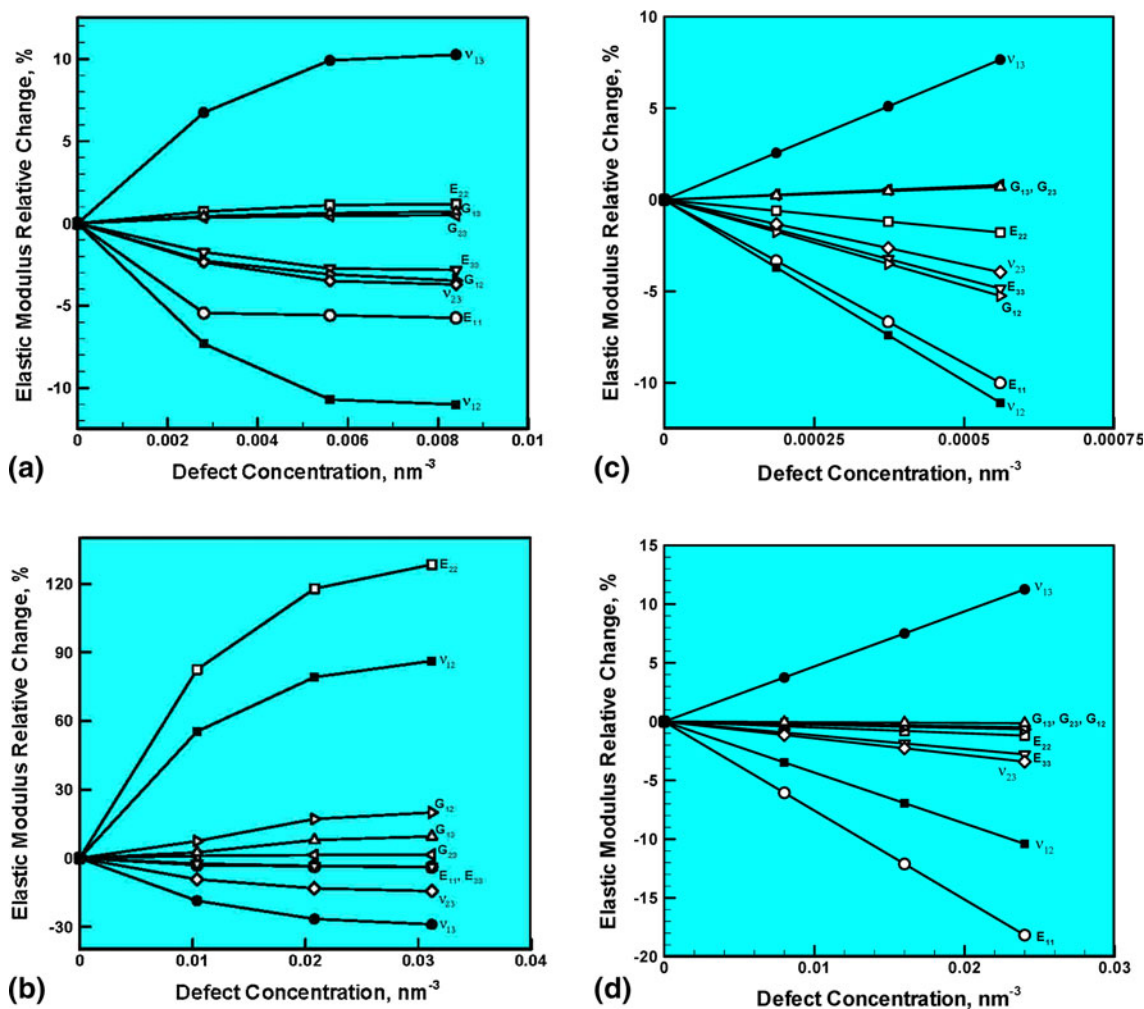


Fig. 8 The effect of the concentration of representative defects on the orthotropic elastic stiffness moduli of the PPTA fibrils: (a) isolated -COOH group (a chain-end defect), (b) isolated -SO₃H group (a side-group defect), (c) isolated mobile H₂SO₄ molecules (an interstitial defect), and (d) a defect band (a planar defect)

analysis can only yield (orientation-dependent) mechanical properties of the fibrils. Hence, to obtain the corresponding fiber mechanical properties, averaging/homogenization of the fibril properties should be employed. However, as will be shown later, to more accurately account for the effect of prior axial-torsion on the longitudinal properties of the PPTA fibers, additional molecular-level computational cells containing bi-fibrils will have to be constructed and analyzed.

Since the work presented in this section includes the effects of the presence, type, and concentration of various topological/crystallographic defects, and the effect of the prior axial compression and/or torsion on the single PPTA fiber longitudinal-tensile strength, the corresponding results are presented and discussed within separate sections (each dealing with a particular case of the fibril crystallinity and prior deformation).

4.1 Perfect PPTA Subjected to Axial Compression

As established earlier, since the computational cells utilized in the present work reside within the fibrils, the molecular-level computational results obtained, after being subjected to the aforementioned post-processing procedure, could only reveal the mechanical properties of the fibrils. Furthermore, as mentioned earlier, the stiffness and strength properties yielded by the post-processing procedures are defined within a Cartesian coordinate system which is attached to the crystal structure of the PPTA fibrils.

4.1.1 Elastic Stiffness Tensor. The aforementioned post-processing procedure yielded the following nine orthotropic elastic moduli for the perfect PPTA-crystal structure: $E_{11} = 105.3$ GPa, $E_{22} = 2.0$ GPa, $E_{33} = 31.3$ GPa, $G_{12} = 0.9$ GPa, $G_{13} = 5.6$ GPa, $G_{23} = 2.6$ GPa, $\nu_{12} = 0.46$, $\nu_{13} = 0.147$, and $\nu_{23} = 0.15$. These values are found to be nearly insensitive (maximum variation found is approximately $\pm 0.1\%$) for different sizes of the PPTA computational cell. It should be recalled that the following material-based orientation of the coordinate system was used: (a) coordinate axis x_1 is aligned with the fibril longitudinal direction, (b) coordinate axis x_2 is aligned with the PPTA sheet-normal direction, and (c) coordinate axis x_3 is aligned with the corresponding in-sheet orthogonal direction.

Application (and recovery) of up to 5% of the prior axial compression was found not to have a measurable effect on the values of these moduli. Examination of the molecular structure before and after the application of longitudinal compression, as will be shown below, confirmed that no microstructural permanent changes were induced by the prior longitudinal compression.

4.1.2 Longitudinal Tensile Strength. The procedure for calculation of the fibril longitudinal tensile strength was described in section 3.5. This procedure, in the case of virgin perfectly crystalline PPTA, yielded a fairly repeatable value of the fibril tensile longitudinal strength of approx. 6.38 ± 0.03 GPa. The longitudinal tensile strength, in this case, was found to be controlled by the progressive loss of the intra-sheet hydrogen bonds.

Application (and recovery) of up to 5% of the prior axial compression was found not to have a measurable effect on the value of the longitudinal tensile strength. To rationalize this finding, PPTA-fibril molecular-level microstructure was examined before, during and after the application of the axial compression. An example of the results examined is depicted in Fig. 6(a) and (b). The results displayed in Fig. 6(a) pertain to

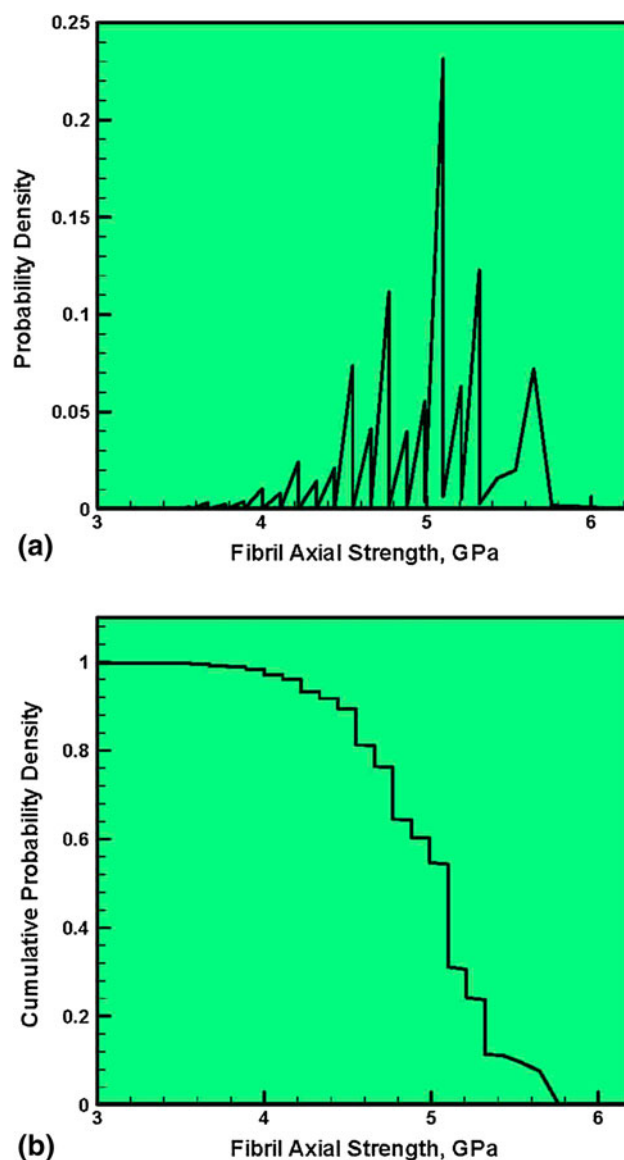


Fig. 9 (a) Virgin defective PPTA-fibril longitudinal-tensile strength probability density function and (b) the corresponding cumulative distribution function determined in the present work using all-atom molecular-level computational analyses

the microstructure before deformation, while Fig. 6(b) shows the microstructure under axial compressive strain of -0.05 . The microstructure obtained upon removal of the compressive strain is practically identical to the one displayed in Fig. 6(a), and, hence, is not shown. Examination of the results displayed in Fig. 6(a) and (b) shows that, under axial compression, PPTA sheets undergo buckling. However, these microstructural changes are completely removed upon unloading/strain recovery. The absence of residual changes in the PPTA-crystal microstructure is the reason that no measurable changes were detected in the longitudinal tensile strength after the application of the prior axial compression.

4.2 Perfect PPTA Subjected to Axial Torsion

4.2.1 Elastic Stiffness Tensor. As in the case of the prior compression, application of up to 0.1 simple shear strain (used to mimic axial torsion) was found not to have a measurable

effect on the values of the nine orthotropic elastic moduli in the perfect PPTA crystal, and, as will be shown below, no permanent changes in the material microstructure were induced by the prior axial torsion.

4.2.2 Longitudinal Tensile Strength. As in the case of the prior compression, prior application of up to 0.1 simple shear strain was found not to measurably affect the aforementioned value (6.38 ± 0.03 GPa) of the perfect-PPTA longitudinal-tensile strength. To rationalize this finding, PPTA-fibril molecular-level microstructure was examined before, during, and after the application of the axial torsion (i.e., simple shear). An example of the results examined is depicted in Fig. 7(a) and (b). The results displayed in Fig. 7(a) pertain to the microstructure before deformation, while Fig. 7(b) shows the microstructure under simple shear strain of 0.1. The microstructure obtained upon removal of the simple shear strain is practically identical to the one displayed in Fig. 7(a), and, hence, is not shown. Examination of the results displayed in Fig. 7(a) and (b) shows that, under simple shear, phenylene rings ($C_6H_4(CO)_2$ and $C_6H_4(NH)_2$) within PPTA filaments undergo (non-uniform) rotation. However, these microstructural changes are com-

pletely removed upon unloading/strain recovery. The absence of residual changes in the PPTA-crystal microstructure is the reason that no measurable changes were detected in the longitudinal tensile strength after the application of the prior axial torsion.

4.3 Imperfect PPTA Subjected to Axial Compression

4.3.1 Elastic Stiffness Tensor. As clearly demonstrated in our recent work (Ref 1, 2), the orthotropic elastic stiffness moduli of the PPTA fibrils are affected by the type, size/potency, concentration/number density, and clustering of microstructural/topological defects. While Ref 1, 2 contain the complete results of a comprehensive investigation pertaining to the effects of morphological/crystallographic defects on the PPTA elastic stiffness, only a few representative results are depicted in Fig. 8(a)-(d). Specifically, Fig. 8(a)-(d) shows the effect of a defect from each of the four defect classes, as listed in Table 1. That is, the effect of the concentration of the following defects on the orthotropic elastic stiffness moduli of the PPTA fibrils is depicted: (a) isolated -COOH group

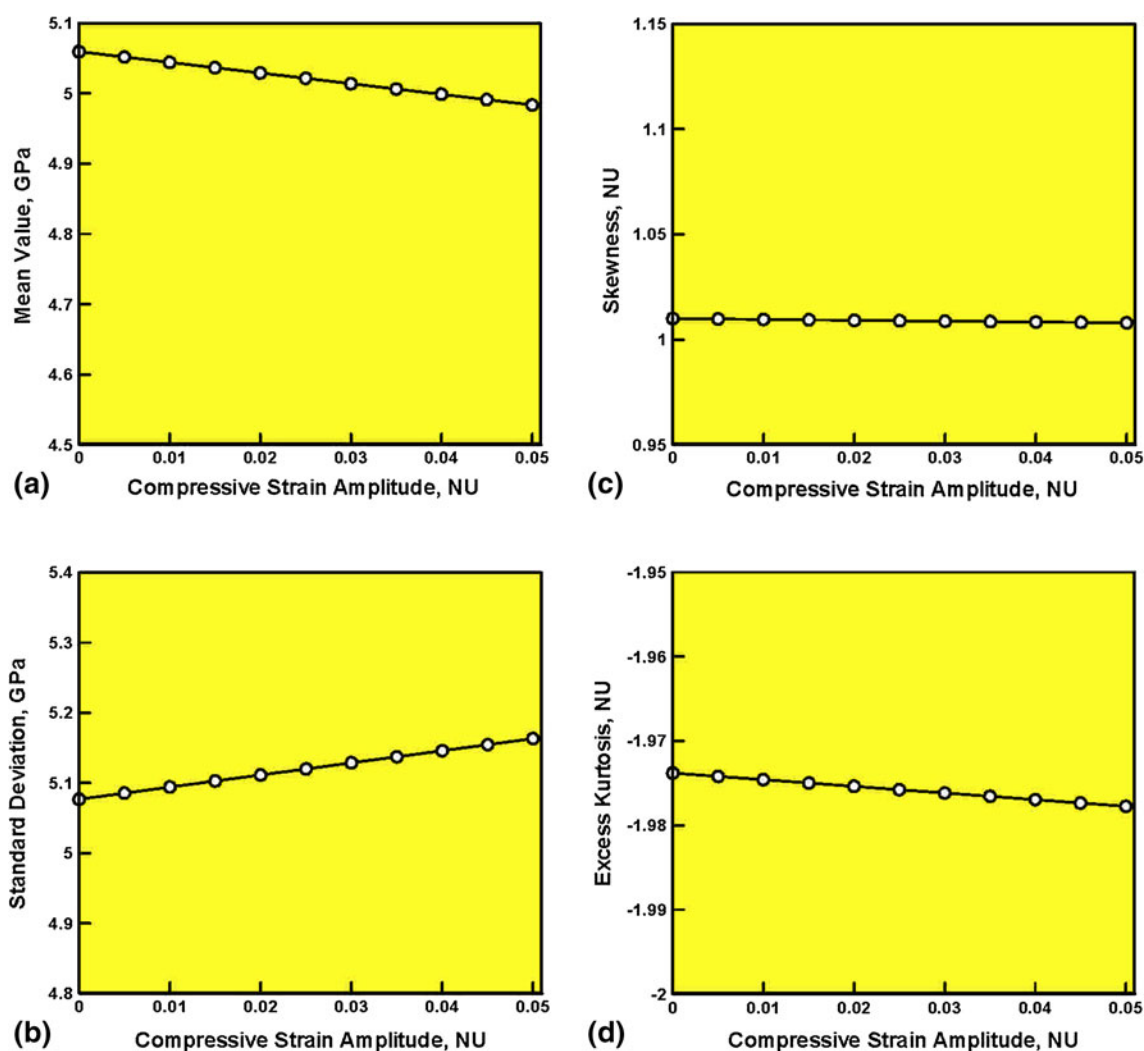


Fig. 10 The effect of prelude axial compressive strain magnitude on the first four moments of the single-fibril longitudinal-tensile-strength probability density function: (a) mean value, (b) standard deviation, (c) skewness, and (d) excess kurtosis

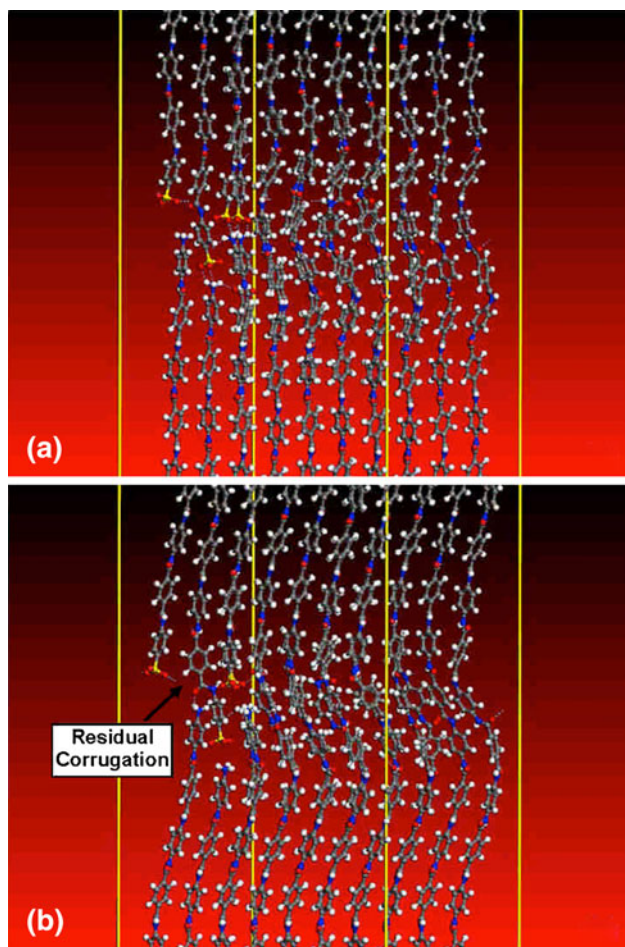


Fig. 11 Molecular-level microstructure in imperfect PPTA crystal: (a) before and (b) after the application and removal of axial compressive strain of -0.05

(a chain-end defect), Fig. 8(a); (b) isolated $-\text{SO}_3\text{H}$ group (a side-group defect), Fig. 8(b); (c) isolated mobile H_2SO_4 molecules (an interstitial defect), Fig. 8(c); and (d) a defect band (a planar defect), Fig. 8(d). It should be noted that the results depicted in Fig. 8(a)-(d) show the defect-induced changes in the respective elastic moduli relative to their aforementioned values in the perfect PPTA structure. Furthermore, it should be noted that the results displayed in Fig. 8(a)-(b), (c), (d) are associated with uncertainties of ± 0.31 , ± 0.55 , and $\pm 0.79\%$, respectively.

Examination of Fig. 8(a)-(d) reveals that: (a) the orthotropic elastic moduli change monotonically with an increase in the defect concentrations; (b) among the elastic moduli, longitudinal normal stiffness (E_{11}) and the inter-sheet shear stiffness (G_{12}) are most strongly affected/compromised by the presence of the chain-end defects, Fig. 8(a); (c) in the case of isolated $-\text{SO}_3\text{H}$ side-group defects, Fig. 8(b), trans-sheet normal stiffness increases strongly due to formation of inter-sheet hydrogen bonds. Figure 8(b) further reveals that the shear moduli G_{12} and G_{13} are also increased due to the formation of inter-sheet hydrogen bonds; (d) the presence of interstitial defects has a highly detrimental longitudinal stiffness reducing effect, Fig. 8(c); and (e) the effect observed in (d) is even more pronounced in the case of defect bands, Fig. 8(d).

Application of up to 5% of the prior axial compression had relatively small (maximum ca. 1%) effect on the values of the nine orthotropic elastic moduli, depicted in Fig. 8(a)-(d). As will be shown below, these changes in the orthotropic elastic moduli were accompanied by relatively small permanent changes in the PPTA single-crystal microstructure.

4.3.2 Longitudinal-Tensile Strength. The analysis of the results obtained using the PPTA computational cells with different types and number densities of morphological/crystallographic defects revealed that the PPTA fibril longitudinal-tensile strength is effectively controlled by the size, composition and structure of the largest (i.e., the most potent) defect or cluster of defects. Due to the stochastic character of the defects present within the fibrils, fibril longitudinal-tensile strength has also been found to be a stochastic quantity, which is in agreement with several experimental reports (Ref 23-25). In our recent work (Ref 2), a procedure was developed for the derivation and parameterization of a probability density function for the longitudinal-tensile strength of PPTA fibrils. Details of this procedure will not be repeated here. However, it should be noted that the procedure involved the following simplifications and steps: (i) an assumption that the defect distribution within the fibrils follows the principles of a Poisson point process; (ii) introduction of the concept of “volume of influence” in order to establish a criterion for declaring closely spaced individual defects a single (high-potency) defect cluster; (iii) use of the defect concentrations associated with the prototypical PPTA fiber fabrication conditions; (iv) post-processing of the molecular-level calculation results; and (v) application of statistical probability analysis to the post-processed molecular-level computational results.

Application of this procedure to the results obtained in the present work yielded the virgin-defective crystal PPTA fibril longitudinal-tensile-strength probability density and cumulative density functions depicted, respectively, in Fig. 9(a) and (b). The mean value of the virgin-defective PPTA longitudinal tensile strength, computed as the first moment of the probability density function displayed in Fig. 9(a), is found to be ~ 5.06 GPa. This value is in reasonably good agreement with the measured PPTA-fibril longitudinal-tensile strength [typically found to be in a 3-5 GPa range (Ref 23, 26)]. This finding suggests that the present computational procedure can reasonably well account for the experimental observations regarding the PPTA fibril longitudinal-tensile strength. The cumulative density function displayed in Fig. 9(b) defines the probability that the PPTA fibril longitudinal-tensile strength is higher than or equal to a given (lower bound) value and this type of function is often used in probabilistic/reliability based design analyses (Ref 27-30).

Application of the prior axial compression was found to change the longitudinal-tensile-strength probability density function (PDF). It should be noted that the term “non-virgin” will be used to denote PPTA fibrils subjected to prior longitudinal compression or axial torsion. The extent of change in the longitudinal-tensile-strength of non-virgin-defective PPTA fibrils was found to continuously increase with an increase in the magnitude of the axial compressive strain. For simplicity, the effect of the prior axial compression on the longitudinal-tensile strength has been quantified by assessing the corresponding changes in the first four PDF moments. For a PDF, $f(x)$, the n th moment is defined as:

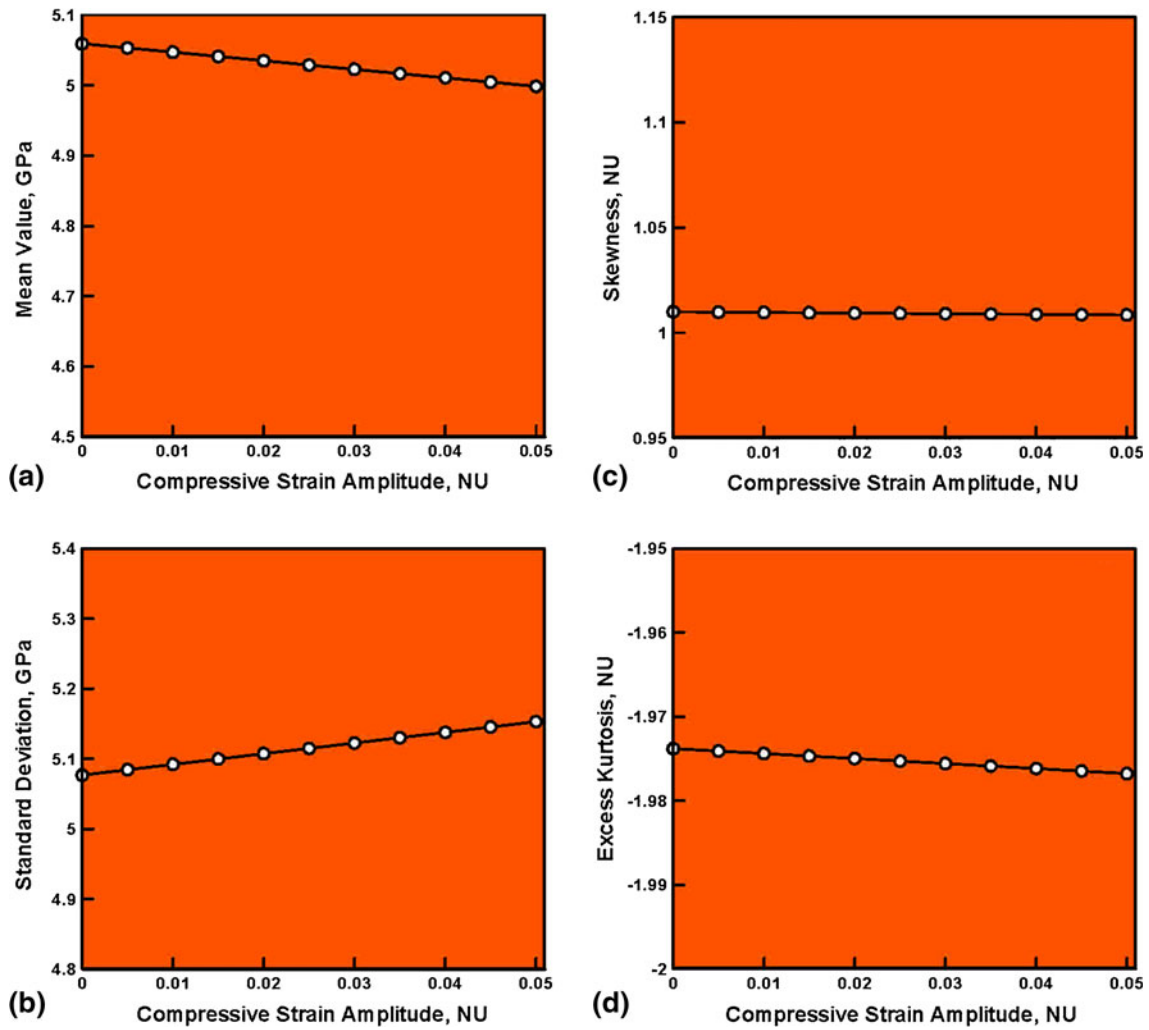


Fig. 12 The effect of preludial simple shear strain magnitude on the first four moments of the single-fibril longitudinal-tensile-strength probability density function: (a) mean value, (b) standard deviation, (c) skewness, and (d) excess kurtosis

$$M_n = \int_{-\infty}^{\infty} x^n f(x) dx,$$

where the longitudinal tensile strength is used, in the present case, as variate x . The first four PDF moments, in ascending order, are: (a) the mean (a measure of the average value of the variate); (b) the variance (a measure of the width of the distribution about its mean). In place of the variance, its square root, called the standard deviation, was monitored in the present work; (c) the skewness (a measure of the asymmetry of the PDF about its mean), defined as the third moment normalized by the third power of the standard deviation; and (d) the (excess) kurtosis (a measure of the slenderness of the distribution, compared to the normal distribution of the same variance), obtained by subtracting 3 (the kurtosis of the standard normal distribution) from the fourth moment normalized by the fourth power of the standard deviation. The longitudinal-tensile-strength PDF, for the virgin-defective-PPTA, displayed in Fig. 9(a) is characterized by the following values of these parameters: mean = 5.06 GPa;

standard deviation = 5.08 GPa (indicates a relatively large spread in the longitudinal tensile strength); skewness = 1.01 (indicates a longer tail of data to the left of the mean); and excess kurtosis = -1.97 (indicates that the current PDF is shorter and wider than the corresponding normal distribution with identical standard deviation).

The effect of the magnitude of the prior longitudinal-compressive strain on the first four longitudinal-tensile-strength PDF-moment-based parameters is depicted in Fig. 10(a)-(d), respectively. Examination of the results displayed in these figures reveals that prior axial compression has relatively small effect on these parameters, changing them by a maximum of ca. 1.5%. These changes include a reduction in the mean value, a slight increase in the standard deviation, and effectively no changes in the skewness and excess kurtosis.

To rationalize the aforementioned findings, residual changes in the microstructure of the PPTA fibrils caused by prior axial compression are investigated in defective PPTA crystals. An example of the results examined is depicted in Fig. 11(a) and (b). The results displayed in Fig. 11(a) pertain to the microstructure before deformation, while Fig. 11(b) shows the microstructure after the application and subsequent removal

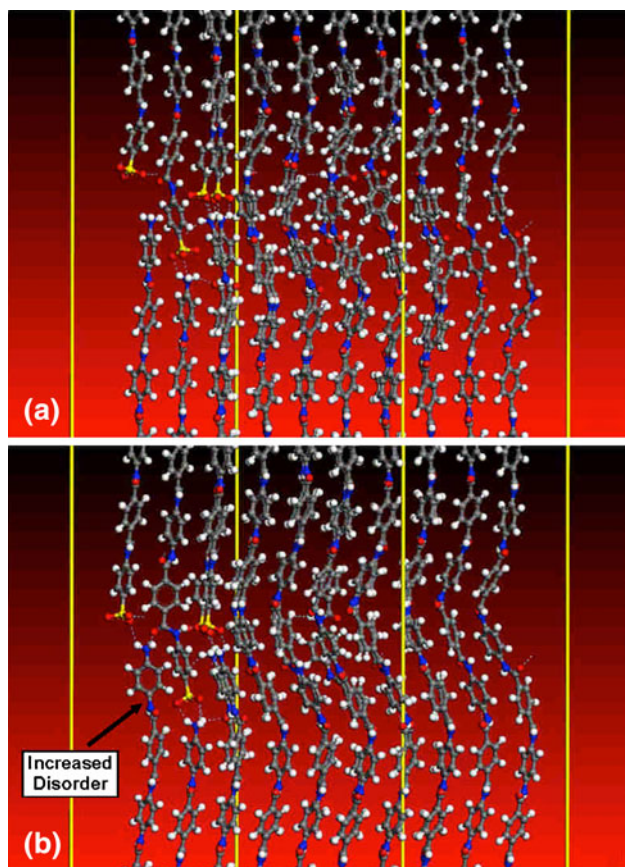


Fig. 13 Molecular-level microstructure in imperfect PPTA crystal: (a) before and (b) after the application and removal of axial torsion strain of 0.1

of axial compression strain of -0.05 . Examination of the results displayed in Fig. 11(a) and (b) shows that the temporary application of axial compression gives rise to some permanent changes in the PPTA microstructure. Specifically, under axial compression, PPTA sheets are found to contain residual corrugation upon the removal of the axial compressive strain. In addition, a reduction in the number of hydrogen bonds (denoted as dashed lines) is observed. These residual changes in the PPTA-crystal microstructure are a likely reason that the prior axial compression causes changes in the PPTA-fibril longitudinal-tensile strength (or, more precisely, in the four statistical parameters characterizing the distribution of this quantity).

4.4 Imperfect PPTA Subjected to Axial Torsion

4.4.1 Elastic Stiffness Tensor. As in the case of the prior compression, application of up to 0.1 simple shear strain had relatively small (maximum ca. 1%) effect on the values of the nine orthotropic elastic moduli, depicted in Fig. 6(a)-(d). As will be shown below, these changes in the orthotropic elastic moduli were accompanied by relatively small permanent changes in the PPTA single-crystal microstructure.

4.4.2 Longitudinal Tensile Strength. The effect of the prior axial-torsion strain on the first four longitudinal-tensile-strength PDF-moment-based parameters is depicted in Fig. 12(a)-(d), respectively. Examination of the results

displayed in these figures reveals that prior axial torsion has relatively small effect on these parameters, changing them by a maximum of ca. 1.2%. These changes are associated with a reduction in the mean value, a slight increase in the standard deviation, and effectively no changes in the skewness and excess kurtosis.

To rationalize the aforementioned findings, residual changes in the microstructure of the PPTA fibrils caused by prior simple shear are investigated in defective PPTA crystals. An example of the results examined is depicted in Fig. 13(a) and (b). The results displayed in Fig. 13(a) pertain to the microstructure before deformation, while Fig. 13(b) shows the microstructure after the application and subsequent removal of simple shear strain of 0.1. Examination of the results displayed in Fig. 13(a) and (b) shows that the application of simple shear gives rise to some permanent changes in the PPTA microstructure. Specifically, under axial torsion, an increase in the extent of disorder is observed, particularly in the region adjacent to the defect. This disorder is accompanied by a reduction in the number of hydrogen bonds. These residual changes in the PPTA-crystal microstructure are a probable reason that the prior axial torsion causes the aforementioned changes in the four statistical parameters which characterize the distribution of the PPTA-fibril longitudinal-tensile strength.

4.5 PPTA Bi-fibril Subjected to Axial Compression/Torsion

The results presented and discussed in the previous sections are in reasonable agreement with the experimental findings (Ref 15) relative to the effect of prior axial compression on the longitudinal tensile strength. That is, preludial axial compression has relatively little effect on the residual longitudinal axial strength of the PPTA fibrils. However, DeTeresa et al. (Ref 15) found that axial torsion has a profound degrading effect on the residual longitudinal-tensile strength of the PPTA fibrils. This finding is not matched by the present molecular-level computational results. One of the potential reasons for this discrepancy is that DeTeresa et al. (Ref 15) found that prior axial torsion gives rise to pronounced fibrillation type of damage, i.e., damage which involves decohesion/debonding of the adjacent fibrils within the fiber. Since all the molecular-level computational analyses carried out so far involved single-crystalline PPTA material (i.e., the material residing within a single PPTA fibril), these analyses are incapable of predicting the fibrillation damage mechanism. To overcome this limitation of the present analysis, several new computational cells containing PPTA bi-crystals are constructed and subjected to axial torsion. An example of such a cell, prior to the application of the axial torsion, is shown using the standard ball-and-stick representation in Fig. 14(a). For improved clarity, the same computational cell is depicted in Fig. 14(c) using the line representation.

Figure 14(b) and (d) show the same cell, in the standard ball-and-stick and the line representations, respectively, after the application and removal of simple shear strain of 0.1. The results displayed in Fig. 14(b) and (d) clearly show damage/delamination occurring in the inter-fibril boundary region. In addition, some reduction in the number of hydrogen bonds is also observed in this region. These microstructural changes can lead to complete decohesion/separation of the adjacent fibrils within the PPTA fiber, as observed experimentally in the work of DeTeresa et al. (Ref 15). A schematic of the PPTA fiber

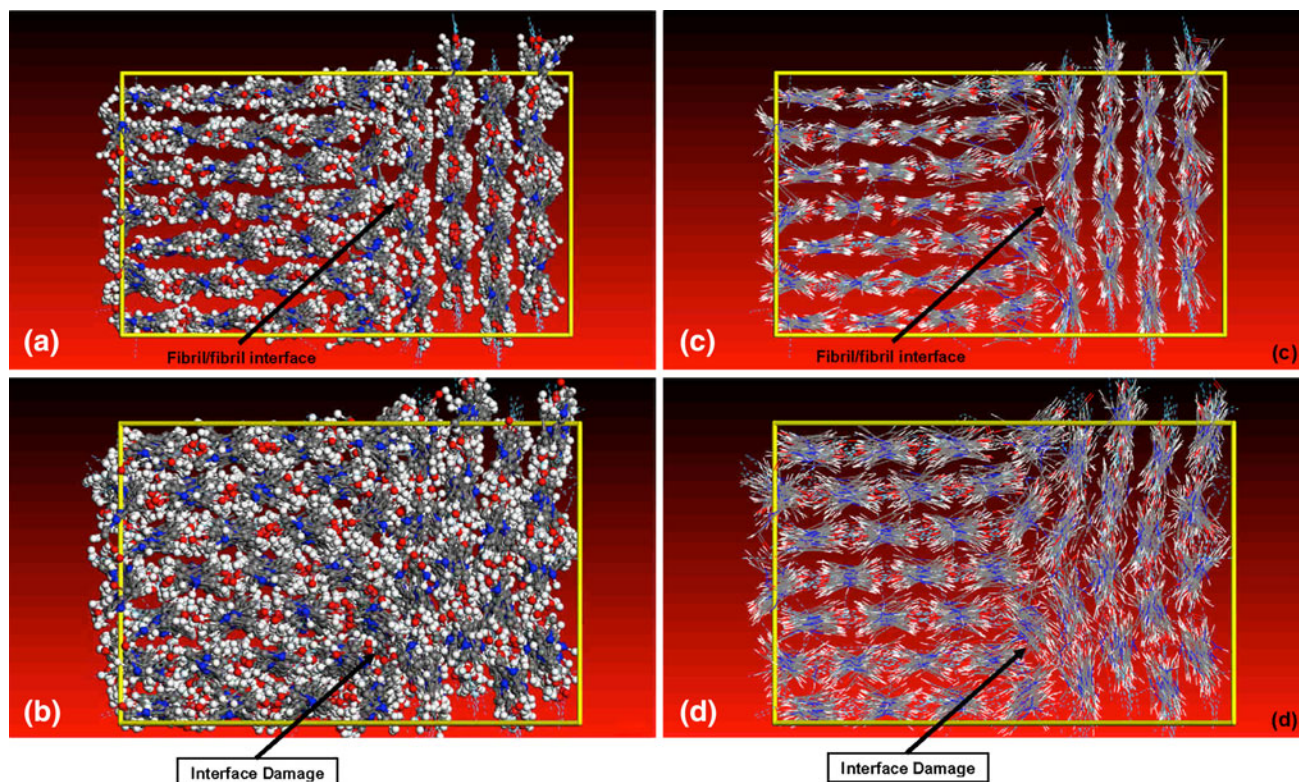


Fig. 14 Molecular-level microstructure in PPTA bi-crystal: (a) and (c) before; and (b) and (d) after the application and removal of axial torsion strain of 0.1. Ball-and-stick representation is used in (a) and (b), while line representation is used in (c) and (d)

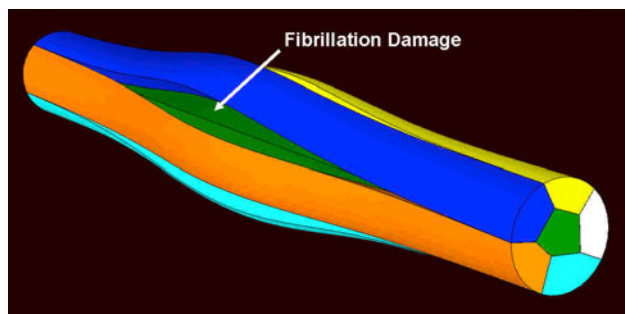


Fig. 15 A schematic of the fibrillation damage/failure mode observed in PPTA fibers during torsion

morphology containing a region damaged by the fibrillation mechanism is depicted in Fig. 15.

The effect of the prior axial-torsion strain on the first four longitudinal-tensile-strength PDF-moment-based parameters for the PPTA bi-fibrils is depicted in Fig. 16(a)-(d), respectively. Examination of the results displayed in these figures reveals that prior axial torsion has a significantly larger effect than in the case of PPTA imperfect single crystals on these parameters, changing them by as much as 5%. These changes include: (a) a reduction in the mean value by as much as 4.8%, (b) an increase in the standard deviation by as much as 5%, (c) a smaller ($<1\%$) decrease in the skewness, and (d) also a smaller ($<0.7\%$) decrease in the excess kurtosis. These findings suggest that prior axial torsion applied to the PPTA bi-fibrils causes an increase in the number density, size and

potency of the morphological and crystallographic defects (e.g., the loss of inter-fibril cohesion, as seen in Fig. 14b, d). These changes in the PPTA bi-fibril microstructure are, hence, a probable cause for the observed reduction in the residual longitudinal-tensile strength and the operation of the fibrillation damage/failure mechanism.

The results presented above pertain to the case of imperfect PPTA bi-fibrils subjected to axial torsion. Application of axial compression to the same bi-fibrils did not produce major residual changes in the material microstructure and, hence, no significant reductions in the longitudinal-tensile strength were observed. These findings could be readily explained considering the fact that adjacent fibrils can more readily undergo conformal axial compression (which does not yield permanent changes in the material microstructure), while the response of adjacent fibrils to the imposed simple shear could be quite different, resulting in strain discontinuity across the fibril-fibril interface (and in the formation of morphological/crystallographic defects in the interfacial region).

4.6 Fiber Properties

The analyses presented in the previous section yielded the elastic stiffness and the longitudinal-tensile properties of single- and bi-fibril structures. However, it is the PPTA fibers which are used in the fabrication of different protective structures and, hence, one is generally interested in determining the fiber properties (from the computed single- and bi-fibril properties). The procedures used for the calculation of the PPTA fiber properties are briefly overviewed in the remainder of this section.

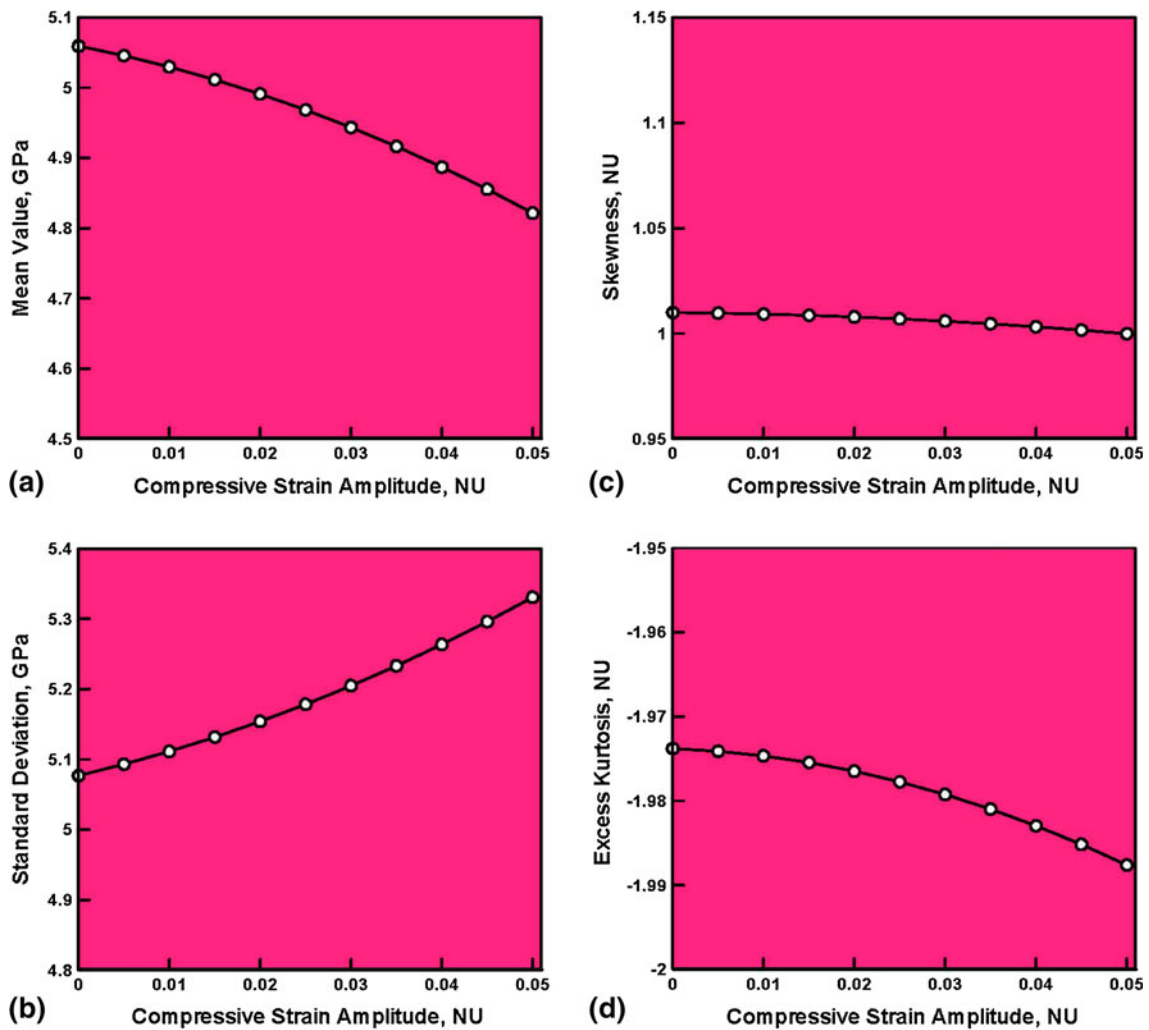


Fig. 16 The effect of preludial simple shear strain magnitude on the first four moments of the bi-fibril longitudinal-tensile-strength probability density function: (a) mean value; (b) standard deviation; (c) skewness; and (d) excess kurtosis

4.6.1 Elastic Stiffness Tensor. Before the elastic stiffness properties of PPTA fibers can be determined, one must compute the mean values of the PPTA-fibril elastic stiffness moduli. To predict the mean values of the orthotropic elastic moduli in fibrils of the commercially produced PPTA fibers, the following deterministic procedure was employed: (a) for each of the microstructural/topological defects analyzed in the present work, a mean value of the defect concentration (and its typical range) under prototypical PPTA-fiber fabrication conditions is assessed using the available open-literature reports. More detailed description of this assessment procedure can be found in our prior work (Ref 2); (b) due to the very low values of the defect concentrations, it is assumed that the combined effects of different defects can be obtained using a simple linear-superposition procedure; and (c) the effect of individual defects on the fibril orthotropic elastic moduli is assumed to be represented by the results displayed in Fig. 8(a)-(d).

It should be noted that the mechanical properties (including elastic stiffness) of the individual PPTA fibrils are not generally experimentally measured and the relevant data are not available in the open literature. Instead, single fibers are often tested and the fiber mechanical property data are available. It should be recalled that the longitudinal axes of the fibrils and the fiber are

effectively coincident and, hence, one expects that the fibril longitudinal properties are fairly representative of the fiber longitudinal properties. In other words, to provide the grounds for validation of the present computational model, computed longitudinal Young's modulus E_{11} ($= 105.3 \pm 5.3$ GPa) is compared with its experimental fiber-based counterpart ($= 84.62 \pm 4.18$ GPa) (Ref 26). This comparison suggests that the present computational analysis reasonably well accounts for the longitudinal stiffness behavior of the PPTA fibrils/fibers.

As far as the PPTA fiber transverse normal stiffness is concerned, it is also generally measured (Ref 26). However, since in the transverse direction, fibrils can have a variety of crystallographic orientations, a direct comparison between the computed fibril- and measured fiber-transverse-stiffnesses is not possible. Instead, one has to first apply an averaging/homogenization procedure to the computed transverse stiffness for the fibril in order to determine an "effective" transverse stiffness for the fiber. Then, a computation/experiment comparison regarding the fiber transverse-stiffness properties can be carried out. In our recent work (Ref 4), an averaging procedure was proposed which can yield: (a) a constant-strain Voigt-type upper bound; and (b) a constant-stress Reuss-type lower bound for the fiber transverse normal stiffness. This procedure applied

to the perfect-PPTA-fibril results obtained in the present work yielded a lower bound of 2.9 GPa and an upper bound of 6.5 GPa for the PPTA fibril/fiber transverse Young's modulus, $E_{22} = E_{33}$. This range is in fair agreement with its experimental counterpart $E_{22} = 1.34 \pm 0.35$ GPa (Ref 26). It should also be noted that the procedure mentioned above converts orthotropic fibril stiffness matrix into the corresponding transversely isotropic fiber stiffness tensor.

It should be recalled that in the present investigation, both the computational cells containing perfectly crystalline and defective PPTA were analyzed, which enables quantification of the effects of various microstructural/topological defects on the fibril mechanical properties (via the use of the procedures described in section 3.5). The inclusion of these defects was found to affect the fiber stiffness properties to the same extent as in the case of PPTA fibrils, Fig. 8(a)-(d).

4.6.2 Longitudinal-Tensile Strength. In accordance with Fig. 5(b), fibers are considered as assemblies of nearly parallel fibrils bonded, in the lateral direction, mainly via van der Waals forces. As established earlier, while PPTA sheets within all fibrils of a given fiber run parallel to the fiber axis, the orientation distribution of the sheet normals, within a plane normal to the fiber axis, is typically assumed to be of a random nature. Consequently, the transverse strength of the PPTA fibers is expected to be an average of the same quantity found in PPTA fibrils. A detailed procedure for calculation of the PPTA-fiber transverse strength was developed and applied in our recent work (Ref 4) and, hence, will not be repeated here (since the main focus of the present work is not transverse but rather longitudinal tensile strength). As far as the longitudinal-tensile strength of the fibers is concerned, it is expected to be nearly identical to that of the constituent fibrils. Hence, one should expect that the longitudinal strength of the PPTA fibrils is a stochastic quantity possessing a very similar PDF as its counterpart in the PPTA fibrils and the effect of prior axial compression or axial torsion should have a similar effect on the four aforementioned stochastic parameters.

5. Summary and Conclusions

Based on the results obtained in the present work, the following summary remarks and main conclusions can be drawn:

1. The effect of prior axial compression and/or axial torsion on the residual longitudinal-tensile strength of PPTA fibrils and fibers is investigated computationally using all-atom molecular statics and dynamics simulation methods.
2. In order to ensure that the computational model accurately accounts for the microstructure encountered in PPTA fibrils/fibers, consideration is given to the presence of various crystallographic/topological defects and their clusters.
3. Due to the stochastic nature of the defects type, concentration/number density and size/potency, the PPTA fibril/fiber longitudinal-tensile strength was found to be a statistical quantity possessing a characteristic PDF.
4. Application of the prior axial compression or axial torsion to the PPTA imperfect single-crystalline fibrils has been found to degrade their longitudinal tensile strength

and to modify the associated probability density function (but only slightly).

5. Introduction of the fibril/fiber interfaces into the computational analyses revealed that prior axial torsion can induce major changes in the material microstructure, causing significant reductions in the PPTA-fiber longitudinal-tensile strength and appreciable changes in the associated probability density function.

Acknowledgments

The material presented in this paper is based on work supported by the Army Research Office (ARO) research contract entitled "Multi-length Scale Material Model Development for Armor-grade Composites", Contract Number W911NF-09-1-0513. The authors are indebted to Dr. Larry Russell of ARO for his continuing support and interest in the present work.

References

1. M. Grujicic, W.C. Bell, P.S. Glomski, B. Pandurangan, C.F. Yen, and B.A. Cheeseman, Filament-Level Modeling of Aramid-based High Performance Structural Materials, *J. Mater. Eng. Perform.*, 2011, **20**, p 1401–1413
2. M. Grujicic, W.C. Bell, P.S. Glomski, B. Pandurangan, C.-F. Yen, and B.A. Cheeseman, Multi-length Scale Computational Derivation of Kevlar® Yarn-level Material Model, *J. Mater. Sci.*, 2011, **46**, p 4787–4802
3. M. Grujicic, B. Pandurangan, J.S. Snipes, C.-F. Yen, and B.A. Cheeseman, Multi-Length Scale Enriched Continuum-Level Material Model for Kevlar®-Fiber Reinforced Polymer-Matrix Composites, *J. Mater. Eng. Perform.*, 2013, **22**, p 681–695
4. M. Grujicic, S. Ramaswami, J. S. Snipes, R. Yavari, G. Lickfield, C.-F. Yen, and B. Cheeseman, Molecular-Level Computational Investigation of Mechanical Transverse Behavior of p-phenylene terephthalamide (PPTA) Fibers, *Multidiscip. Model. Mater. Struct.*, 2013 (accepted)
5. M. Grujicic, G. Arakere, T. He, W.C. Bell, B.A. Cheeseman, C.-F. Yen, and B. Scott, A Ballistic Material Model for Cross-Plied Unidirectional Ultra-High Molecular Weight Polyethylene Fiber-Reinforced Armor-Grade Composites, *Mater. Sci. Eng., A*, 2008, **498**, p 231–241
6. M. Grujicic, G. Arakere, T. He, W.C. Bell, P.S. Glomski, and B.A. Cheeseman, Multi-scale Ballistic Material Modeling of Cross-plyed Compliant Composites, *Composites B*, 2009, **40**, p 468–482
7. M. Grujicic, P.S. Glomski, T. He, G. Arakere, W.C. Bell, and B.A. Cheeseman, Material Modeling and Ballistic-resistance Analysis of Armor-Grade Composites Reinforced with High-Performance Fibers, *J. Mater. Eng. Perform.*, 2009, **18**, p 1169–1182
8. M. Grujicic, W.C. Bell, G. Arakere, T. He, X. Xie, and B.A. Cheeseman, Development of a Meso-scale Material Model for Ballistic Fabric and its Use in Flexible-Armor Protection Systems, *J. Mater. Eng. Perform.*, 2010, **19**, p 22–39
9. S.L. Kwolek, Optically Anisotropic Aromatic Polyamide Dopes, U.S. Patent 3,671,542, 1972
10. E.I. du Pont, Technical brochure, "Weight Savings for Aircraft using Kevlar Aramid Fiber," 1983
11. H. Blades, Dry-Jet Wet Spinning Process, U.S. Patent 3,767,756, 1973
12. M. Grujicic, G. Arakere, H.K. Nallagatla, W.C. Bell, and I. Haque, Computational Investigation of Blast Survivability and Off-road Performance of an Up-armored High-Mobility Multi-purpose Wheeled Vehicle (HMMWV), *J. Automob. Eng.*, 2009, **223**, p 301–325
13. M. Grujicic, B. Pandurangan, U. Zecevic, K.L. Koudela, and B.A. Cheeseman, Ballistic Performance of Alumina/S-2 Glass-Reinforced Polymer-Matrix Composite Hybrid Lightweight Armor Against Armor Piercing (AP) and Non-AP Projectiles, *Multidiscip. Model. Mater. Struct.*, 2007, **3**, p 287–312
14. M. Grujicic, B. Pandurangan, K.L. Koudela, and B.A. Cheeseman, A Computational Analysis of the Ballistic Performance of Light-Weight Hybrid-Composite Armors, *Appl. Surf. Sci.*, 2006, **253**, p 730–745

15. S.J. DeTeresa, S.R. Allen, R.J. Farris, and R.S. Porter, Compressive and Torsional Behaviour of Kevlar 49 Fibre, *J. Mater. Sci.*, 1984, **19**, p 57–72
16. M.G. Dobb, D.J. Johnson, and B.P. Saville, Compressional Behaviour of Kevlar Fibres, *Polymer*, 1981, **22**, p 960–965
17. M. Cheng, W. Chen, and T. Weerasooriya, Mechanical Properties of Kevlar® KM2 Single Fiber, *J. Eng. Mater. Technol.*, 2005, **127**, p 197–203
18. H. Sun, COMPASS: An Ab-Initio Force-Field Optimized for Condensed-Phase Applications-Overview with Details on Alkane and Benzene Compounds, *J. Phys. Chem. B*, 1998, **102**, p 7338–7364
19. H. Sun, P. Ren, and J.R. Fried, The Compass Force Field: Parameterization and Validation for Phosphazenes, *Comput. Theor. Polym. Sci.*, 1998, **8**, p 229–246
20. MSI, Forcefield Engines, *CDDiscover*, September 1997, Molecular Simulations Inc., San Diego, CA, 1997
21. Materials. Studio, *Discover Theory Manual*, Accelrys Inc., Princeton, NJ, 2009
22. M. Grujicic, T. He, H. Marvi, B.A. Cheeseman, and C.-F. Yen, A Comparative Investigation of the Use of Laminate-level Meso-Scale and Fracture-Mechanics Enriched Meso-scale Composite-Material Models in Ballistic Resistance Analyses, *J. Mater. Sci.*, 2010, **45**, p 3136–3150
23. J.A. Newell and M.T. Sagendorf, Experimental Verification of the End-effect Weibull Model as a Predictor of the Tensile Strength of Kevlar 29 (Poly p-phenylene terephthalamide) at Different Gage Lengths, *High Perform. Polym.*, 1999, **11**, p 297–305
24. L.W. Steenbakkers and H.D. Wagner, Elasticity and Mechanical Breakdown of Kevlar 149 Aramid Fibers by Probabilistic Approach, *J. Mater. Sci. Lett.*, 1988, **7**, p 1209–1212
25. W.F. Knoff, A Modified Weakest-link Model for Describing Strength Variability of Kevlar Aramid Fibers, *J. Mater. Sci.*, 1987, **22**, p 1024–1030
26. M. Cheng, W. Chen, and T. Weerasooriya, Experimental Investigation of the Transverse Mechanical Properties of a Single Kevlar® KM2 fiber, *Int. J. Solids Struct.*, 2004, **41**, p 6215–6232
27. M. Grujicic, G. Arakere, W.C. Bell, H. Marvi, H.V. Yalavarthy, B. Pandurangan, I. Haque, and G.M. Fadel, Reliability-Based Design Optimization for Durability of Ground-Vehicle Suspension-System Components, *J. Mater. Eng. Perform.*, 2010, **19**, p 301–313
28. M. Grujicic, V. Sellappan, T. He, N. Seyr, A. Obieglo, M. Erdmann, and J. Holzleitner, Total Life-Cycle Based Materials Selection for Polymer Metal Hybrid Body-In-White Automotive Components, *J. Mater. Eng. Perform.*, 2009, **18**, p 111–128
29. M. Grujicic, G. Arakere, B. Pandurangan, A. Hariharan, C.-F. Yen, B.A. Cheeseman, and C. Fountzoulas, Statistical Analysis of High-Cycle Fatigue Behavior of Friction Stir Welded AA5083–H321, *J. Mater. Eng. Perform.*, 2011, **20**, p 855–864
30. M. Grujicic, G. Arakere, A. Hariharan, and B. Pandurangan, A Concurrent Product-Development Approach for Friction-Stir Welded Vehicle-Underbody Structures, *J. Mater. Eng. Perform.*, 2012, **21**, p 437–449